Additive Manufacturing 13 (2017) 14–36

Contents lists available at ScienceDirect

Additive Manufacturing

journal homepage: www.elsevier.com/locate/addma

Full Length Article

Predictive modeling and optimization of multi-track processing for laser powder bed fusion of nickel alloy 625☆

Luis E. Criales[a], Yiğit M. Arısoy[a], Brandon Lane[b], Shawn Moylan[b], Alkan Donmez[b], Tuğrul Özel[a,*]

[a] Rutgers University, Department of Industrial & Systems Engineering, NJ, USA
[b] National Institute of Standards and Technology, Gaithersburg, MD, USA

ARTICLE INFO

Article history:
Received 26 April 2016
Received in revised form
21 September 2016
Accepted 7 November 2016
Available online 14 November 2016

Keywords:
Selective Laser Melting
Nickel alloy 625
Finite Element Method
Powder Metals
Temperature
Meltpool

ABSTRACT

This paper presents an integrated physics-based and statistical modeling approach to predict temperature field and meltpool geometry in multi-track processing of laser powder bed fusion (L-PBF) of nickel 625 alloy. Multi-track laser processing of powder material using L-PBF process has been studied using 2-D finite element simulations to calculate temperature fields along the scan and hatch directions for three consecutive tracks for a moving laser heat source to understand the heating and melting process. Based on the predicted temperature fields, width, depth and shape of the meltpool is determined. Designed experiments on L-PBF of nickel alloy 625 powder material are conducted to measure the relative density and meltpool geometry. Experimental work is reported on the measured density of built coupons and meltpool size. Statistically-based predictive models using response surface regression for relative density, meltpool geometry, peak temperature, and time above melting point are developed and multi-objective optimization studies are conducted by using genetic algorithm and swarm intelligence.

1. Introduction

Laser powder bed fusion (L-PBF) additive manufacturing in which metal powder is fused layer-by-layer to directly fabricate metal parts of predetermined geometry, involves melting and fusing selected regions of powder material by scanning and hatching the surface of a powder layer with a small-diameter laser beam (~100 μm) have been quickly expanding applications requiring complex geometries in difficult-to-process metals such as nickel-based alloys [29,19]. However, insufficient process understanding is a major obstacle in attaining consistency in fabricated part density, structural integrity, and dimensional quality [5,22].

L-PBF parameters for most common type may machines include: laser power (P), laser wavelength (λ), laser beam spot diameter (d), scan strategy rotation (SSR), scan velocity (v_s), stripe width (w), stripe overlap, hatch or track distance (h), and layer thickness (s) (Fig. 1). The length of a single track is the stripe width plus the stripe overlap. The laser is turned off between processing tracks. Typically, maximum available power, wavelength, and beam spot diameter for the laser are unique to the L-PBF machine, cannot be modified. On the other hand, laser power, scan velocity, hatch distance, and layer thickness can be modified to increase or decrease the *energy density* for controlling the powder fusion. These process parameters alongside powder material properties should be studied together to gain further process insight under a physics-based modeling framework.

In this work, the 2-D laser melting of powder metal during multi-track processing is simulated using a Finite Element Method (FEM)-based program developed in Matlab since development of a 3-D model would be computationally expensive for multi-track processing simulations. Also, the solution is partially extended to 3-D via two 2-D solutions, in order to calculate the temperature field laterally on the surface of the powder bed and vertically into the depth of the powder bed. Two important conclusions are drawn from the resulting temperature field throughout the duration of the process: a) a history of the meltpool geometry, and b) the time spent above the melting temperature for each location of the powder bed. Most researchers who have attempted to optimize process

☆ Official contribution of the National Institute of Standards and Technology (NIST); not subject to copyright in the United States. The full descriptions of the procedures used in this paper require the identification of certain commercial products. The inclusion of such information should in no way be construed as indicating that such products are endorsed by NIST or are recommended by NIST or that they are necessarily the best materials, instruments, software or suppliers for the purposes described.

* Corresponding author at: 96 Frelinghuysen Road, Piscataway, NJ 08854, USA.
E-mail address: ozel@rutgers.edu (T. Özel).

http://dx.doi.org/10.1016/j.addma.2016.11.004
2214-8604/

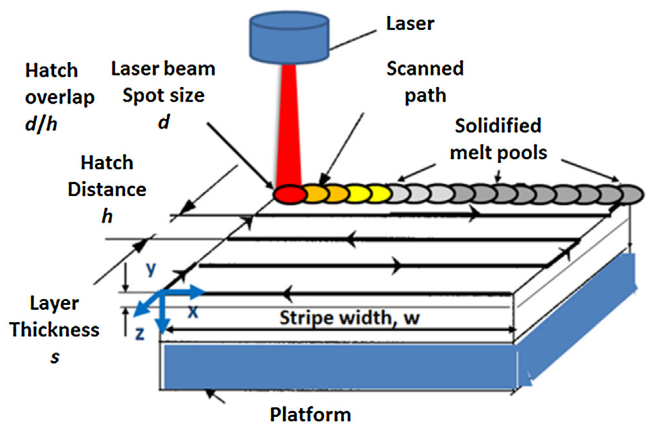

Fig. 1. L-PBF process variables [8].

parameters use predicted meltpool geometry as the key output [16,12,1] but no attention has been paid to utilizing the time spent in liquid phase as a factor related to remelting of adjacent tracks. The connection between the temperature profile and resulting microstructure has not been extensively studied [15,7,28] and most work in literature uses commercial FEM software with limitations [23,14,11]. In this study, physics-based L-PBF models are developed, and simulation predictions are compared against the experiments. Later, process models are developed by utilizing experimental results and simulation predictions under the scheme of response surface methodology and employed in multi-objective optimization of process parameters for various conflicting objectives.

2. Physics-Based Modeling of L-PBF

The purpose of physics-based modeling is to calculate the temperature filed during the L-PBF process. The temperature distribution can be calculated using a numerical solution approach by means of solving the heat equation [8]. The general 3-D heat convection-diffusion equation can be as:

$$\rho C_p \frac{\partial T}{\partial t} = \frac{\partial}{\partial x}\left(k\frac{\partial T}{\partial x}\right) + \frac{\partial}{\partial y}\left(k\frac{\partial T}{\partial y}\right) + \frac{\partial}{\partial z}\left(k\frac{\partial T}{\partial z}\right) + q \tag{1}$$

where ρ is the density, C_p is the isobaric specific heat, T is the material temperature, k is the thermal conductivity, and q is the volumetric heat by assuming that the velocity of the liquid medium in the meltpool is negligible when high velocities above ~100 mm/s are utilized [13]. Solving this equation is computationally costly, and with adequate assumptions, the problem can be simplified to a 2-D problem. The temperature is first considered as a function of time and of two space variables which represent the scanning direction (x) and the hatching direction (y), respectively, while the conduction into the depth (z) direction is not considered.

$$\rho C_p \frac{\partial T}{\partial t} = \frac{\partial}{\partial x}\left(k\frac{\partial T}{\partial x}\right) + \frac{\partial}{\partial y}\left(k\frac{\partial T}{\partial y}\right) + q \tag{2}$$

Solving at $z = 0$, the temperature field is obtained at the powder bed surface. The heat transfer inside the material occurs through conduction. Radiation effects are not a significant source of heat loss. Furthermore, 2-D temperature field can be considered as a cross-section of the full 3-D profile to reduce the 3-D model into 2-D models where the meltpool is the main focus of the model. Hence the problem is defined in the XZ- and YZ- planes as:

$$\rho C_p \frac{\partial T}{\partial t} = \frac{\partial}{\partial x}\left(k\frac{\partial T}{\partial x}\right) + \frac{\partial}{\partial z}\left(k\frac{\partial T}{\partial z}\right) + q \tag{3}$$

$$\rho C_p \frac{\partial T}{\partial t} = \frac{\partial}{\partial y}\left(k\frac{\partial T}{\partial y}\right) + \frac{\partial}{\partial z}\left(k\frac{\partial T}{\partial z}\right) + q \tag{4}$$

The temperature at the intersecting line of the XY and XZ planes must be the same in both XY and XZ simulations for the model to be consistent. These 2-D heat equations are used to solve two fundamentally different problems with proper use boundary conditions.

2.1. Material Properties

In the simulation model, thermo-physical properties of the powder material are defined as functions of the solid (bulk) material properties and as temperature-dependent such as density, $\rho_{bulk}(T)$, and thermal conductivity, $k_{bulk}(T)$ [4,23,14]. Furthermore, powder material density and thermal conductivity are considered as a fraction of the bulk properties:

$$\rho_{powder} = (1-\tau)\,\rho_{bulk} \tag{5}$$

$$k_{powder} = (1-\tau)\,k_{bulk} \tag{6}$$

where τ is the porosity of the packed powder. The packing density of powder is taken as 0.5 in this study.

To model the molten region properly, nonlinearity of specific heat during phase transformation which occurs between the solidus and liquidus temperatures with a net change in enthalpy is considered. The equivalent specific heat is used to model the phase transformation as:

$$C_{eq}(T) = \begin{cases} C_p(T),\ T \le T_s \\ C_p(T) + \dfrac{L_f}{T_l - T_s},\ T_s < T < T_l \\ C_l,\ T \ge T_l \end{cases} \tag{7}$$

where $C_p(T)$ is the specific heat of the solid material before it reaches the solidus temperature, C_l is the specific heat of the material in liquid phase, L_f is the latent heat of fusion of the material, T_s is the solidus temperature, and T_l is the liquidus temperature [27,24]. The heat source is modeled using a Gaussian-like continuous wave laser beam and the z-level is assumed constant. Using the Gaussian distribution for beam intensity [27], the moving heat source on the powder layer surface can be given as:

$$q = (1-R)\frac{2P}{\pi w_o^2} e^{-2\left(r^2/w_o^2\right)} \tag{8}$$

where R is the reflectivity of the material, P is the laser power, w_o is the beam waist size, and r is the distance from the beam center. The laser penetration into powder bed is assumed to be insignificant and the laser energy assumed to be absorbed on the surface.

In the XZ simulation, the y-coordinate is fixed, causing the heat source distribution to be solely a function of x. In the XY case, the region of interest is the surface, where $z = 0$. For the XZ case, the main region of interest is the centerline of the track ($y = 0$). For the YZ case, the regions of interest are the starting and ending point of each track ($x = 0$ and $x = x_{end}$). For each of the plane pairs, the temperature at the intersection of the planes must be the same (Fig. 2). This is accomplished by solving the problem in the XY plane using Neumann boundary conditions, and then using the resulting temperature field as an input to the XZ and YZ simulations together with Dirichlet boundary conditions in a single-direction coupled approach (Table 1).

2.2. Finite element method

The workpiece is represented with a mesh and a numerical scheme is applied to solve the heat equation. The Galerkin method

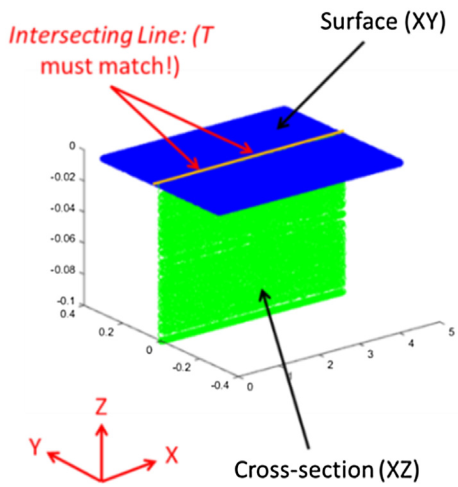

Fig. 2. Illustration of XY-and XZ-planes.

Table 1
Material properties for nickel alloy 625 [18].

T_l [K]	1623
T_s [K]	1563
ρ [kg/m^3]	8440
L_f [kJ/kg]	227
C_p (*T*) [J/kg K]	0.2437 *T* + 338.98
k (*T*) [W/m K]	0.015 *T* + 5.331
R	0.7

is utilized to represent the current continuous problem as a discrete problem which can be written in matrix form [3].

$$\mathbf{C}(T)\dot{\mathbf{T}} + \mathbf{K}(T)\mathbf{T} = \mathbf{q} \tag{9}$$

where **C**(*T*) is the heat capacity matrix, **K**(*T*) is the heat conduction matrix, **T** is the nodal temperature vector, $\dot{\mathbf{T}}$ is the nodal temperature rate vector and **q** is the heat source vector. The heat capacity matrix is a function of both material properties (density, heat capacity) and the shape function matrix, **N**.

$$\mathbf{C}(T) = \int_{\Omega} \rho C_p \boldsymbol{N}^T \boldsymbol{N} d\Omega \tag{10}$$

Similarly, the heat conduction matrix is a function of thermal conductivity and the shape function matrix.

$$\boldsymbol{K}(T) = \int_{\Omega} k \boldsymbol{B}^T \boldsymbol{B} d\Omega \tag{11}$$

where matrix **B** is obtained by taking the partial derivative of the matrix **N** with respect to the spatial coordinates. Furthermore, the heat vector is given as;

$$\boldsymbol{q} = \int_{\Omega} q \boldsymbol{N}^T d\Omega \tag{12}$$

The element shape function for a 2nd order isoparameteric triangle is given as;

$$\boldsymbol{N} = \left[\xi\left(2\xi - 1\right) 4\xi 4\xi\left(1\xi - \eta\right)\eta(2\eta - 1) 4\eta\left(1 - \xi - \eta\right)\left(1 - \xi - \eta\right)\left(2\left(1 - \xi - \eta\right) - 1\right)\right] \tag{13}$$

where ξ and η are two independent variables used to describe the local coordinates of the nodes in each triangular element. Integration over the problem domain is done via Gaussian quadrature, which calculates the function to be integrated at discrete points and adds them together using a weighting function. Since the heat capacity and heat conduction matrices are functions of temperature, they must be recalculated at every time step of the process as the temperature field evolves. Therefore, an implicit approach must be utilized to obtain the temperature field as;

$$\mathbf{C}(T)\left(\frac{\Delta\mathbf{T}}{\Delta t}\right) + \mathbf{K}(T)\mathbf{T}^{t+\Delta t} = \mathbf{q} \tag{14}$$

The phase change temperature region is small so phase transition occurs very quickly. The time step, Δt, must be chosen to be small enough so that solution convergence is obtained and the fast heating and cooling times characteristic of L-PBF can be studied. This is solved iteratively at each time step using the Newton-Raphson method, to obtain the change in the temperature field as;

$$\Delta\mathbf{T} = \left(\Delta t \times \left(\mathbf{C}^{-1}\mathbf{K}\right) + \mathbf{I}\right)^{-1}\left(\Delta t \times \mathbf{C}^{-1}\left(\mathbf{q} - \mathbf{K}\mathbf{T}^{t}\right)\right) \tag{15}$$

Then the new temperature field is calculated as;

$$\mathbf{T}^{t+\Delta t} = \mathbf{T}^{t} + \Delta\mathbf{T} \tag{16}$$

The residual vector **R** is calculated as;

$$\mathbf{R} = \left(\Delta t\left(\mathbf{C}^{-1}\mathbf{K}\right) + \mathbf{I}\right) \times \Delta\mathbf{T} - \Delta t \times \mathbf{C}^{-1}\left(\mathbf{q} - \mathbf{K}\mathbf{T}^{t}\right)\Big) \tag{17}$$

When the norm of **R** is less than the specified error tolerance, the current iteration is completed and the temperature at the following time step is calculated.

2.3. Model geometry and boundary conditions

There are three-tracks considered and the scanning direction is selected as positive *x*-direction. The meshes used and related assumptions are given in Fig. 3. The XY model considers a moving heat source, where the heat is distributed to the elements that fall within the beam area at any time step, based on the relative locations of elements to the beam center. Therefore, **q** is calculated directly from the heat intensity of the laser beam. The heat is applied on these elements internally as a heat source via energy consistent lumping of the laser beam captured by an element's area and the location of each element within the beam. The heat source vector *q*(*x*,*y*,*t*) moving in the *x*-direction is realized by calculating the center position of the laser at time step i + 1, so that $x_{i+1} = v_s \Delta t + x_i$. The 2-D meshes are comprised of 6292, 2192, and 1325 triangular elements for the XY-, XZ-, and the YZ-plane models respectively.

In XZ and YZ simulations, there is no heat source and a Dirichlet boundary condition is applied in order to model the correspondent effect of L-PBF. The XZ plane of interest is given by *y* = 0, meaning that the vertical plane through the center of the laser track is considered, and the YZ plane of interest is given by x = 0+. At each time step of XZ and YZ model simulations, the temperature at the top boundary (*z* = 0), Γ_1, is set equal to the temperature obtained from the XY simulation at the corresponding location.

$$T_{XZ}(x, z=0, t)\,|_{y=0} = T_{YZ}(y, z=0, t)\,|_{x=0+} = T_{XY}(x, y=0, t)\,|_{z=0} \tag{18}$$

This method can only be utilized after a full temperature history at the surface is obtained. Appropriate Neumann boundary conditions are applied on the side boundaries: Γ_2 and Γ_4, while Γ_3 is a Dirichlet boundary for both the XZ and YZ cases. The temperature at the bottom of the powder bed ($z = z_{max}$) is set to 353 K since the platform is heated at 80 °C. The initial temperature is $T_{xz}(x, z, t = 0) = T_{yz}(y, z, t = 0) = 353K$.

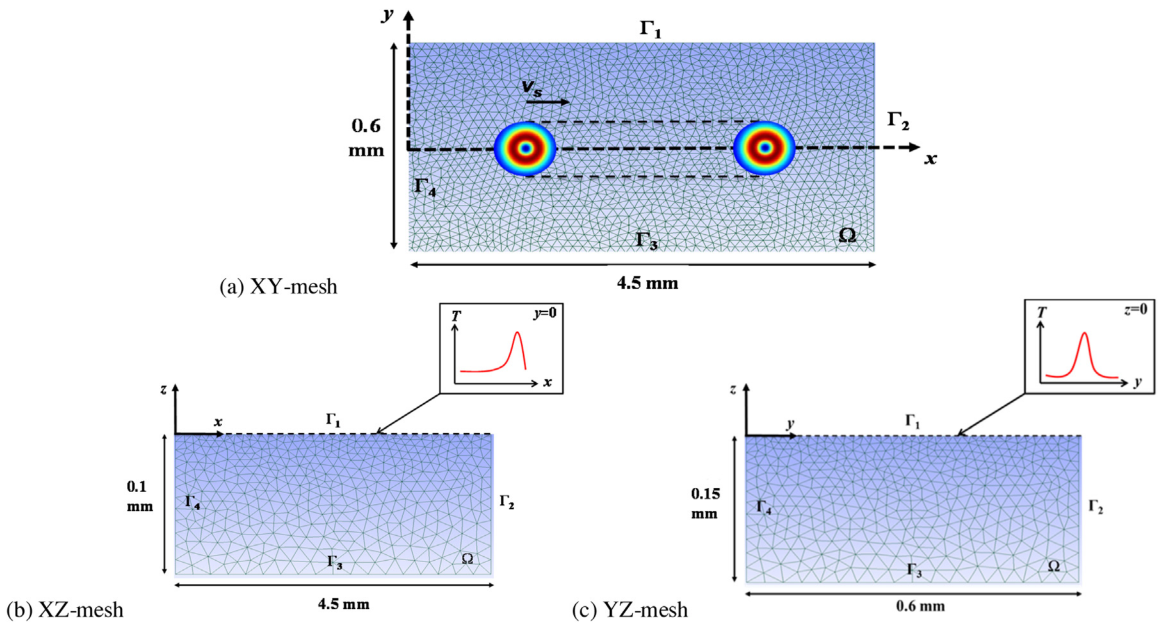

Fig. 3. Illustration of 2-D meshes.

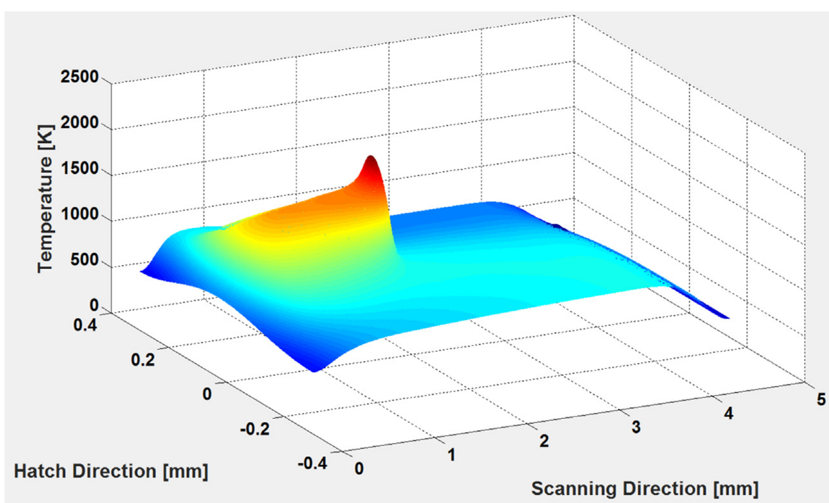

Fig. 4. Temperature on powder bed surface.

2.4. Multi-track simulations

Initially, the physics-based model is applied to a XY-plane simulation of the scanning three tracks, using process parameters: $P = 195$ W, $v_s = 800$ mm/s, $h = 0.10$ mm (default setting in EOS-DMLS machine for nickel alloy 625). The temperature profile on the surface of the powder bed is considered ($z = 0$). Temperatures at any step of the simulation can be represented with a surface plot (Fig. 4).

The evolution of temperature on the powder bed surface can be captured (Fig. 5). Two distinct regions based on current temperature are considered; (i) locations where T is less than the liquidus temperature, indicating that either the material is still in powder form or has re-solidified and (ii) areas where T is greater than the liquidus temperature, indicating full melting of the material. Using this definition, the meltpool geometry is defined (Fig. 6) where liquefied meltpool is shown at a different track. Then, the meltpool geometry is calculated by measuring length and width at its longest and widest points. The increase in meltpool size due to heating of the powder bed by the laser source is clearly observable.

Corresponding 2-D simulations in the XZ-plane were executed by considering three cross-sections of the powder bed: one for each track ($y = -0.10$ mm, 0.0 mm, and 0.10 mm). To obtain temperature distributions in the XZ-plane, simulation uses a profile of temperature vs. scanning direction (x) at a given y from the XY-simulation at each time step. Fig. 7 provides one such temperature profile at the surface of the powder bed ($z = 0$), for $y = +0.10$ mm, the second-track.

Similar behavior is observed in the simulation for XZ-and XY-planes. There is very little melting in the z-direction for the first-track, with maximum temperature rising and meltpool depth increasing as further tracks are processed (Fig. 8). This is due to the increase in heat contained in the workpiece, which preheats the powder before it is scanned, leading to higher temperatures when scanning occurs.

YZ-plane simulations were executed analogously by considering two cross-sections of the powder bed: at each end of the tracks ($x = 0.2$ mm and 4.3 mm). Because this is a multi-track simulation, each of these cross-sections makes it possible to measure meltpool width and depth on each of the three different hatches at different

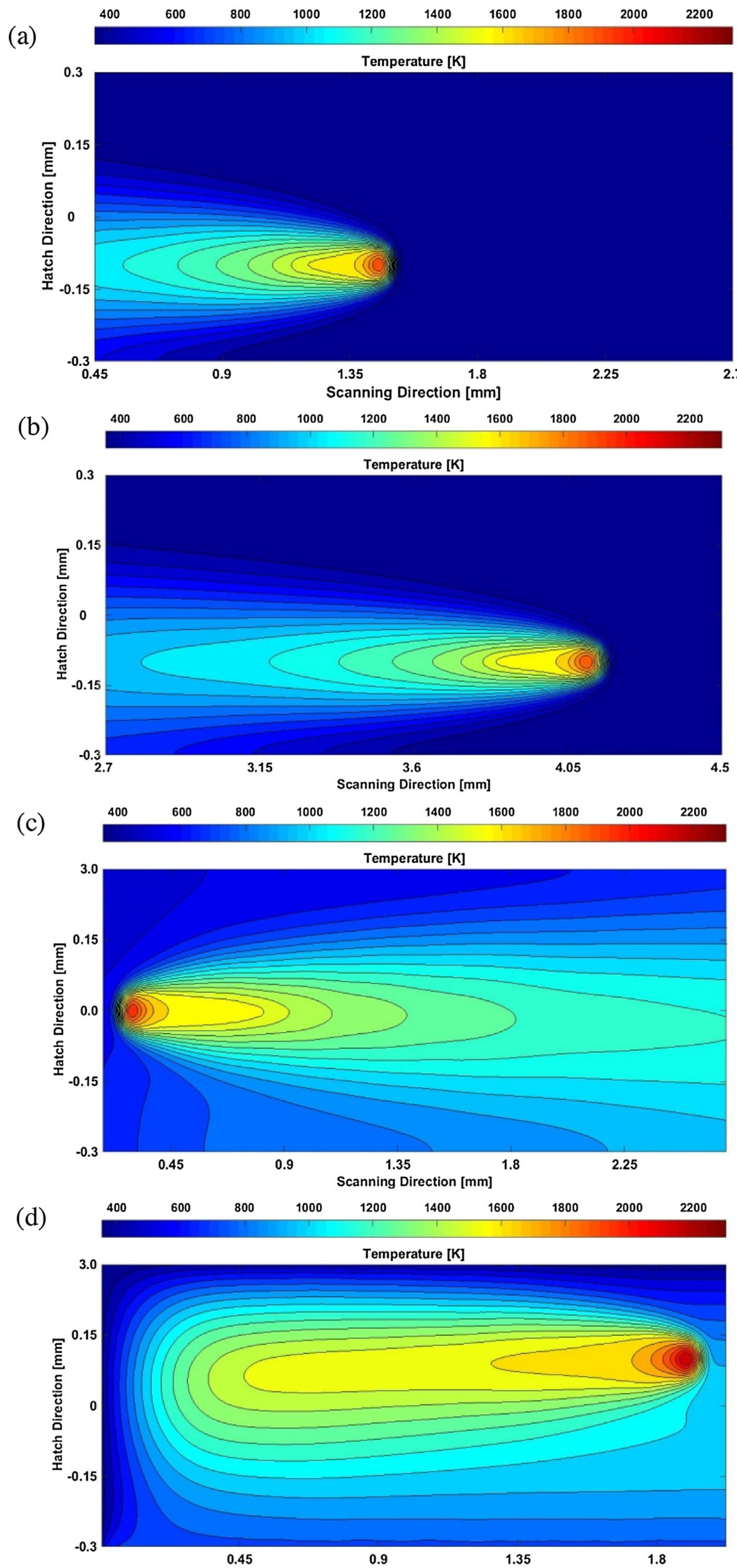

Fig. 5. Surface temperature: (a) first track, $t = 1.66$ ms, (b) first track, $t = 4.98$ ms, (c) second track, $t = 10.50$ ms, (d) third track, $t = 13.29$ ms. ($P = 195$ W, $v_s = 800$ mm/s, $h = 0.10$ mm).

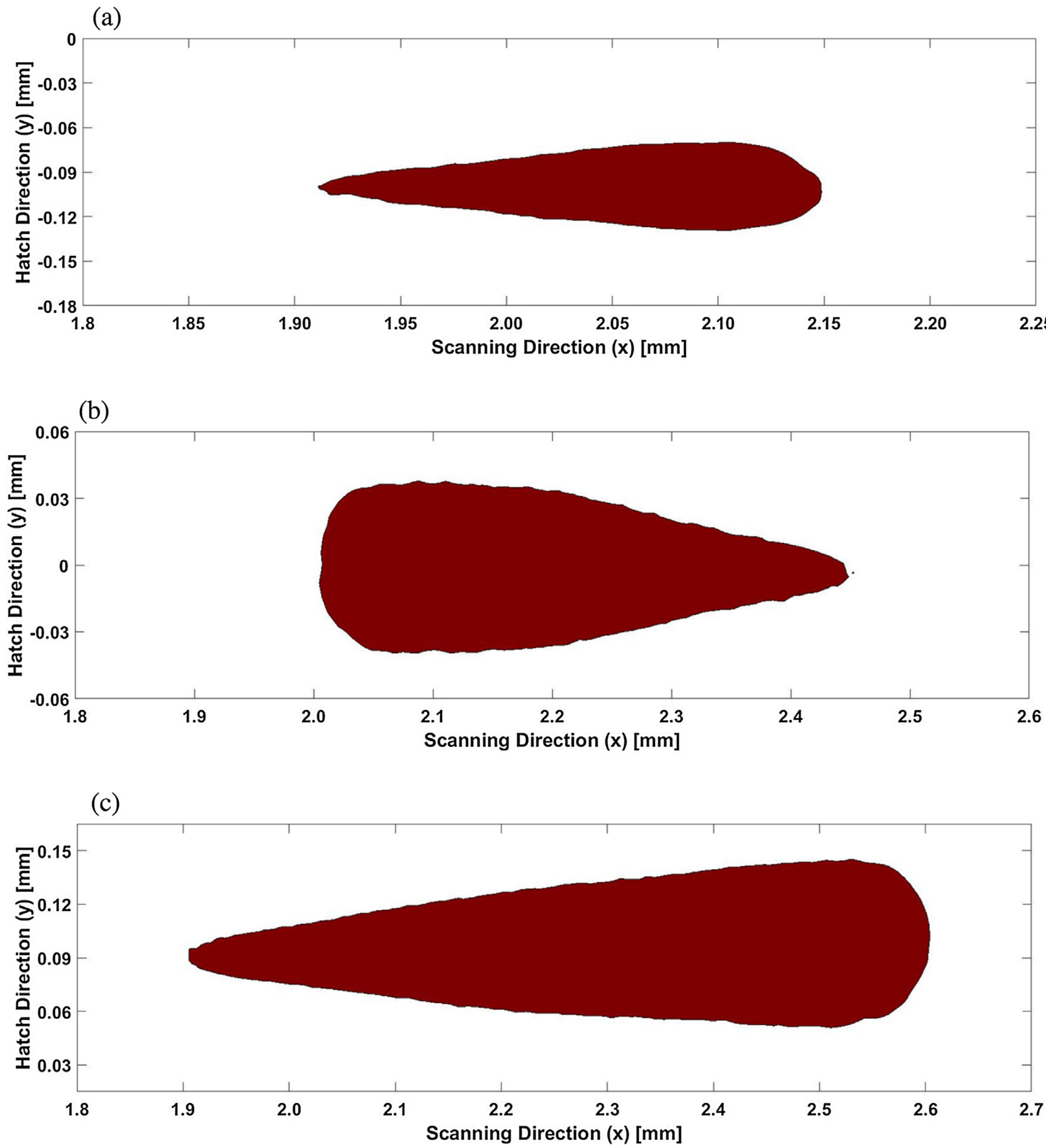

Fig. 6. XY meltpool: (a) first-track (y = −0.1 mm), t = 2.49 ms; (b) second-track (y = 0 mm), t = 8.32 ms; (c) third-track (y = +0.1 mm), t = 14.12 ms. (P = 195 W, v_s = 800 mm/s, h = 0.10 mm).

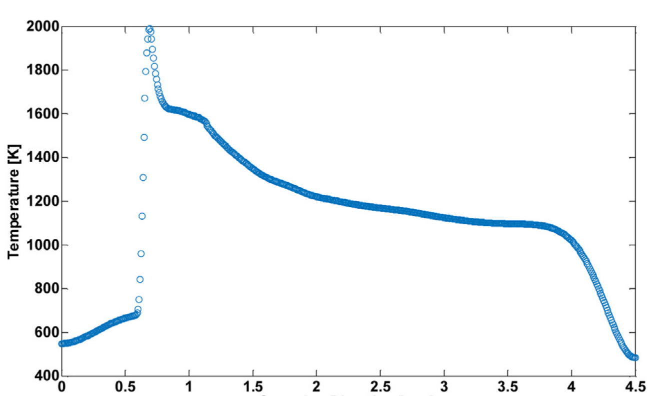

Fig. 7. Temperature profile at y = +0.1 mm, z = 0; t = 14.12 ms.

times of the simulation. The time frame of interest is chosen by considering the time step where the peak temperature is the highest, as this corresponds to the moment when the laser beam is heating this section of the workpiece. This model considers the result of the XY simulation at the z = 0 location as the equivalent of the heat source to obtain temperature distributions in the YZ-plane, following the same procedure that was utilized in the XZ-simulation. Similar behavior is observed in the YZ-plane simulation. There is very little melting in both the y-direction and the z-direction for the first-track, with maximum temperature rising and meltpool width and depth increasing as further hatches are processed (Fig. 9).

Table 2 shows the resulting meltpool length (x_{MP}), width (y_{MP}), and depth (z_{MP}) obtained by combining the results from the three orthogonal plane simulations. It is evident that the meltpool grows in size as a track being processed in L-PBF process. It is also evident that the meltpool width and depth is different at the end of the

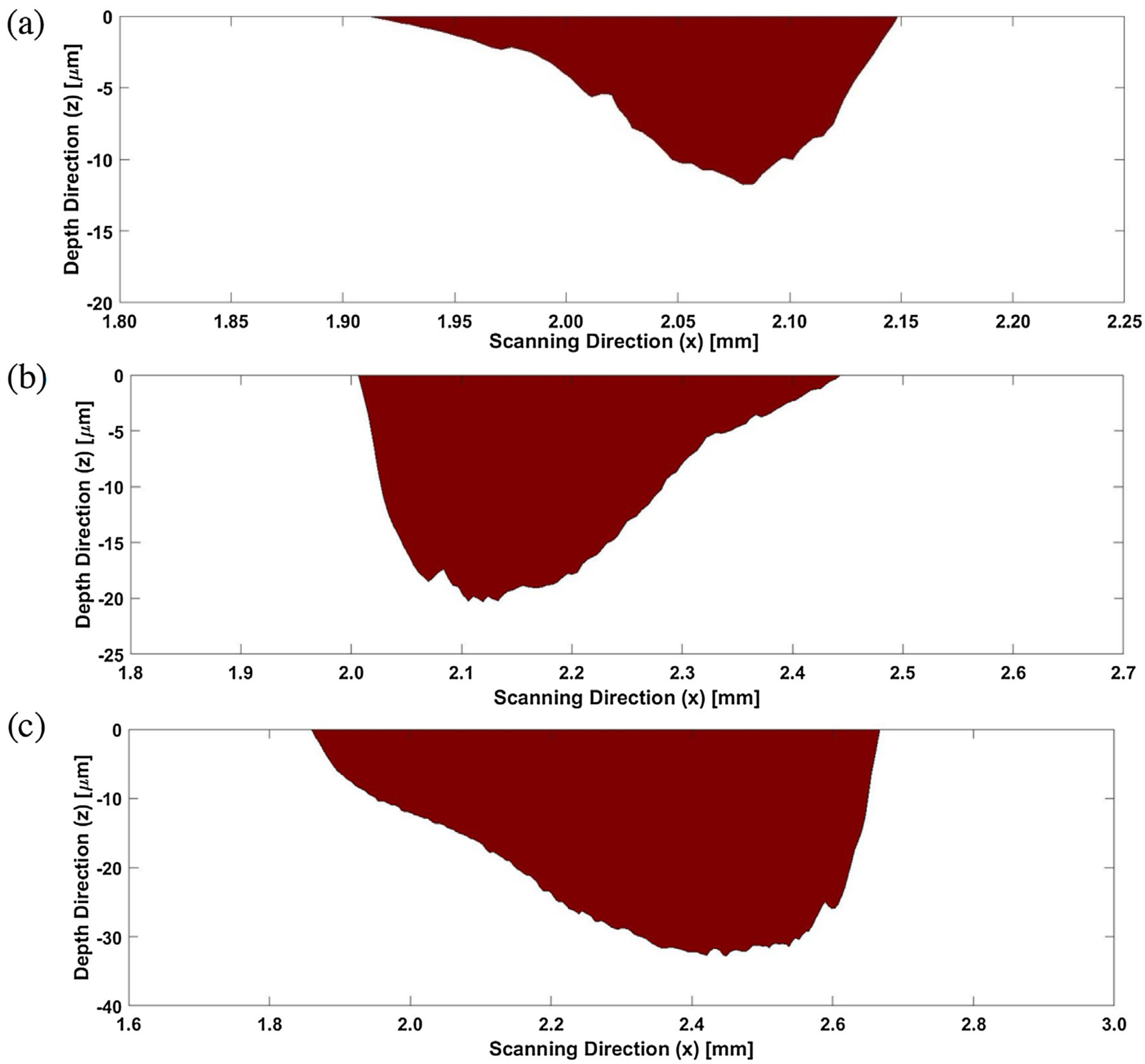

Fig. 8. XZ meltpool: (a) first-track ($y = -0.1$ mm), $t = 2.49$ ms; (b) second-track ($y = 0$ mm), $t = 8.32$ ms; (c) third-track ($y = +0.1$ mm), $t = 14.12$ ms.

Table 2
Calculated meltpool.

Track	Location		Meltpool		
	x [mm]	y [mm]	x_{MP} [μm]	y_{MP} [μm]	z_{MP} [μm]
1	2.00	−0.10	150	85	5
1	4.00	−0.10	168	90	10
2	4.00	0.00	197	137	27
2	2.00	0.00	180	110	21
3	2.00	+0.10	280	152	40
3	4.00	+0.10	250	123	37

second track and at the beginning of the third-track. All material properties are given in Table 1.

3. Experimental Work

In order to verify the model predictions and to develop statistical models an experimental investigation was conducted in collaboration with the National Institute of Standards and Technology (NIST). A commercially available L-PBF machine (EOS M270 Direct Metal Laser Sintering) at NIST was used to fabricate test coupons made out of nickel alloy 625. This machine has a single-mode, continuous wave (CW) ytterbium fiber laser with maximum power of 200 W. The Box-Behnken experimental design [21] suitable for application of response surface methodology was selected due to the size constraints and the limitations hatch distance intervals of 0.01 mm. The test coupons were 16 × 16 mm at the base and 15 mm in height. Each processed layer of powder is composed of four 4-mm wide stripes. Stripe overlap, defined as the area of material in which laser scanning overlaps by consecutive stripes, was 0.1 mm. Therefore, total stripe width or track length was 4.1 mm. Process parameters of $P = 195$W, $v_s = 800$ mm/s, and $h = 0.1$ mm as the "default setting" for L-PBF of nickel alloy 625 were taken as reference point. The three levels selected for the Box-Behnken design were $P = 169$W, 182W, 195W, $v_s = 725$ mm/s, 800 mm/s, 875 mm/s, and $h = 0.09$ mm, 0.10 mm, 0.11 mm. Three additional coupons were built at $P = 195$W, $v_s = 800$ mm/s, $h = 0.10$ mm for control purposes.

In order to investigate the effect of process parameters on the density/porosity of fabricated test coupons, the energy density definition was utilized as a function of power (P), powder layer thickness (s), velocity (v_s), and hatch distance (h);

$$E = \frac{P}{v_s \times h \times s} \tag{19}$$

where layer thickness was fixed as $s = 20$ μm. Therefore, power, velocity, and hatch distance were considered variables in the experiment design together with the scan strategy.

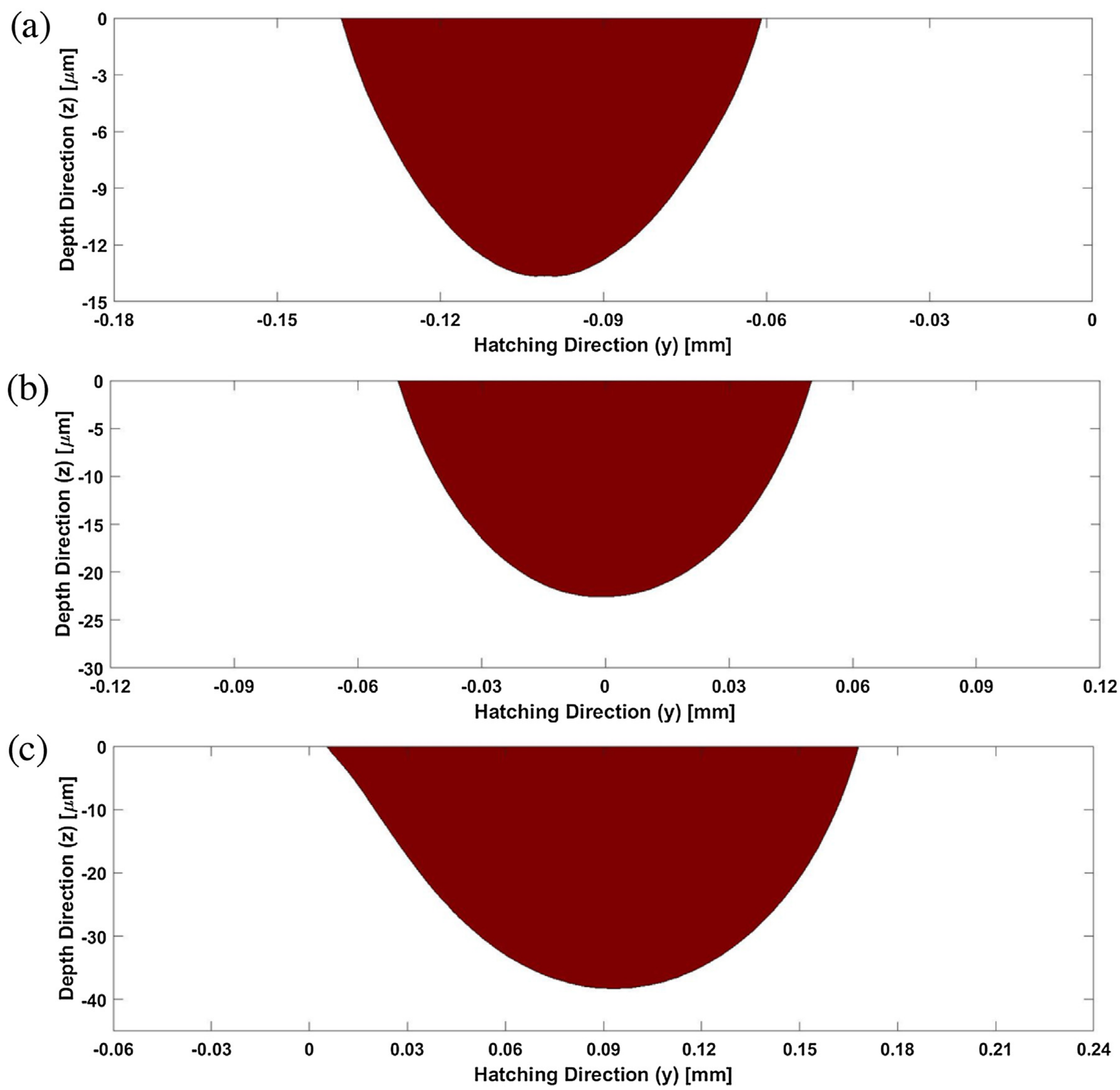

Fig. 9. YZ meltpool: (a) first-track (x = 4.2 mm), t = 4.85 ms; (b) second-track (x = 0.2 mm), t = 10.50 ms; (c) third-track (x = 0.2 mm), t = 11.30 ms.

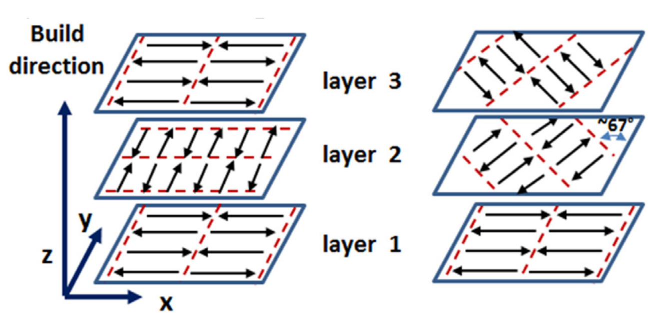

Fig. 10. Scan strategy with 90° (left) and 67° (right) rotation between layers [2].

In the L-PBF process, each layer is formed by selectively fusing the powder material with a given layer thickness. However, consecutive layers are processed slightly differently to ensure a robust build [6]. Specifically, stripe orientation changes from layer to layer by a set amount. Two scan strategies are commonly utilized; 90° and ~67° counterclockwise (CCW) stripe rotation between layers as illustrated in Fig. 10, where red parallel-dashed lines indicate stripe boundaries, while black arrows indicate back-and-forth hatching action on a stripe.

3.1. Relative density measurements

Coupons built were measured for size and mass to determine the density of each coupon. The objective is to determine how close each coupon is to fully dense as measured relative density is defined as;

$$\rho_{rel} = \frac{\rho_{coupon}}{\rho_{bulk}} \times 100\% = \frac{m/V}{\rho_{bulk}} \times 100\% \tag{20}$$

where m and V are the mass and the volume of the coupon, respectively, and ρ_{bulk} is the density of solid nickel alloy 625. A relative density, ρ_{rel} = 100% indicates that the coupon is fully dense. The mass of the coupon was calculated using a weighing scale with an accuracy of 0.001 gr. The mass was measured 5 times for each coupon, and averaged to reduce measurement uncertainty. The volume of the coupon was calculated by measuring the length, width, and height of the coupon using a coordinate measurement machine (CMM) with a length measurement uncertainty of 2.5 μm. Similarly, multiple measurements of each dimension were taken to

Table 3
Measured relative density.

P [W]	v_s [mm/s]	h [mm]	E [J/mm^3]	$SSR = 67^\circ$ ρ_{rel} [%]	$SSR = 90^\circ$ ρ_{rel} [%]
169	875	0.10	96.57	95.2	96.0
195	875	0.10	111.43	98.3	98.7
182	875	0.09	115.56	97.0	97.4
182	725	0.11	114.11	96.0	96.2
195	800	0.11	110.80	98.5	98.5
182	725	0.09	139.46	97.1	97.3
182	800	0.10	113.75	98.1	98.2
182	800	0.10	113.75	98.1	98.2
195	725	0.10	134.48	97.5	97.7
182	800	0.10	113.75	98.1	98.3
182	875	0.11	94.55	96.5	96.8
169	725	0.10	116.55	96.4	96.5
169	800	0.09	117.36	97.5	97.9
169	800	0.11	96.02	96.6	96. 8
195	800	0.09	135.42	99.0	99.2
195	800	0.10	121.88	98.6	98.9
195	800	0.10	121.88	98.5	98.8
195	800	0.10	121.88	98.7	98.8

find the average volume. The bulk density of nickel alloy 625 is 8.440 g/cm^3. Measured relative density values are summarized in Table 3. Note that combining the above mentioned sources of measurement uncertainty results in an expanded density measurement uncertainty ($k = 2$) of about 20 mg/cm^3, which corresponds to about 0.3% expanded uncertainty in determination of relative density.

3.2. Meltpool measurements

Meltpool marks can be analysed to determine important information regarding meltpool geometry [10,11,2,7]. Meltpool geometry data is classified into two types: meltpool dimensions (width and depth) and meltpool shape.

Meltpool width and depth can be measured via digital optical microscopy of the planes that allow a cross-sectional view of the meltpool, i.e. XZ and YZ. It should be noted that there is difficulty in measuring meltpool marks using microscope images especially with the depth measurements on multi-layer parts. It is certain that the subsequent layer will re-melt some of the recently processed layer, likely obscuring some of the meltpool marks by overlapping and increasing uncertainty in these depth measurements. Nevertheless, images were taken using a digital microscope. Image resolution is 1600 pixels × 1200pixels. The length of the meltpool at any specific time cannot be measured due to the continuous nature of the laser scanning process. Therefore, one single continuous track can be observed in the x-direction (Fig. 11). Due to the 90° SSR, XZ and YZ become interchangeable when analyzing meltpool dimensions. Meltpool width and depth can be measured every other layer due to the change in orientation of the scanning direction, which allows a view of the cross-section of the meltpool every other layer.

In order to obtain images where the meltpools could be measured, three of the coupon faces corresponding to XY-, XZ-, and YZ-planes, were electro-polished a total of 50 μm deep. Therefore, measurements were taken at a cross-section very close to the edge of the coupon (Fig. 12).

Note that points A, B, and C will represent consecutive meltpools observed in an image taken of the YZ-plane. The distance between A-B and B-C is the same, and equivalent to one hatch distance. However, there is a discrepancy between the time necessary for the laser to arrive at point B from point A, and the time required to reach point C from point B. Assuming that the laser off-time between hatches is 0.042 ms [17], as measured during coupon building, and the scan velocity is 800 mm/s for a 4.1 mm stripe, it follows that:

$$t_{AB} \approx \frac{2w}{v} = \frac{2\,(4.1\mathrm{mm})}{800\mathrm{mm/s}} = 10.25\mathrm{ms} \tag{21}$$

$$t_{BC} \approx \textit{laser off time} = 0.042\mathrm{ms} \tag{22}$$

Therefore, it takes approximately 10 ms longer for the laser to reach the same x-coordinate location on consecutive hatches, depending on whether this particular location of interest constitutes the beginning or the end of a scanned hatch. This difference in time is considerable, because it allows the powder bed to cool about 10 ms and has an effect on the meltpool dimensions, as shown next.

Two different sizes of meltpools were observed due to the characteristics of the laser scanning process described previously: i) a

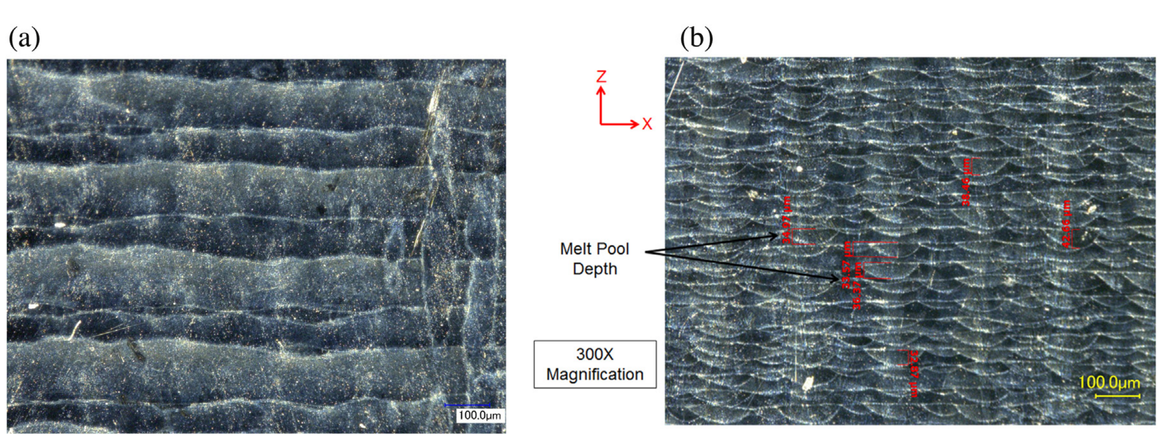

Fig. 11. XY (a) and XZ (b) view (Coupon 35: $P = 195$ W, $v_s = 800$ mm/s, $h = 0.1$ mm).

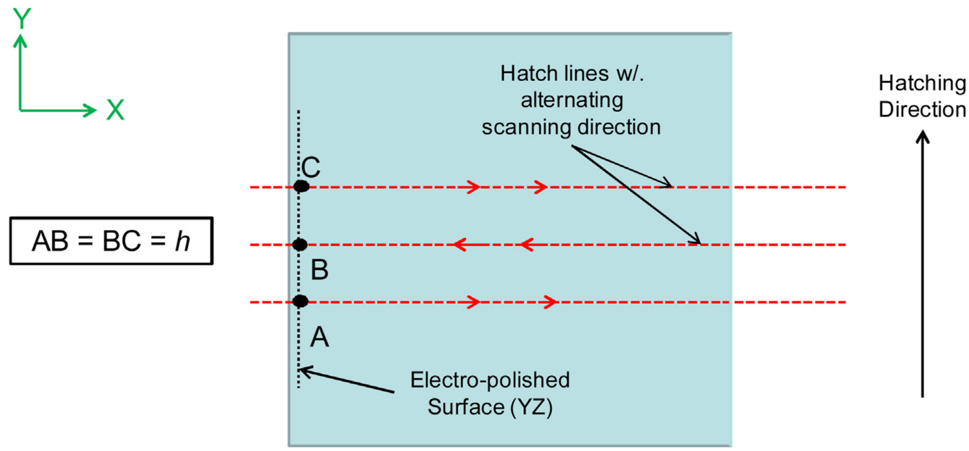

Fig. 12. Location of electro-polished surface.

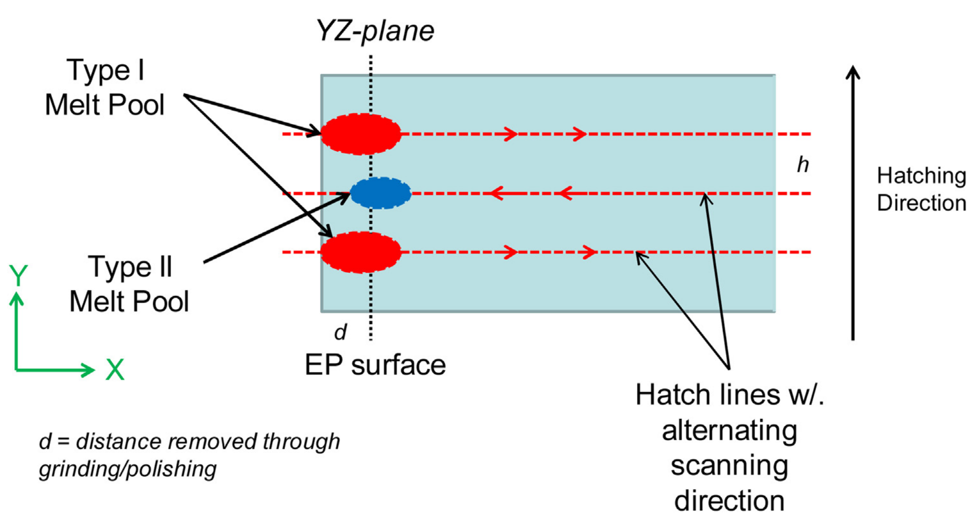

Fig. 13. Definition of Type-I and Type-II meltpools (shape and size of the meltpools are illustrative).

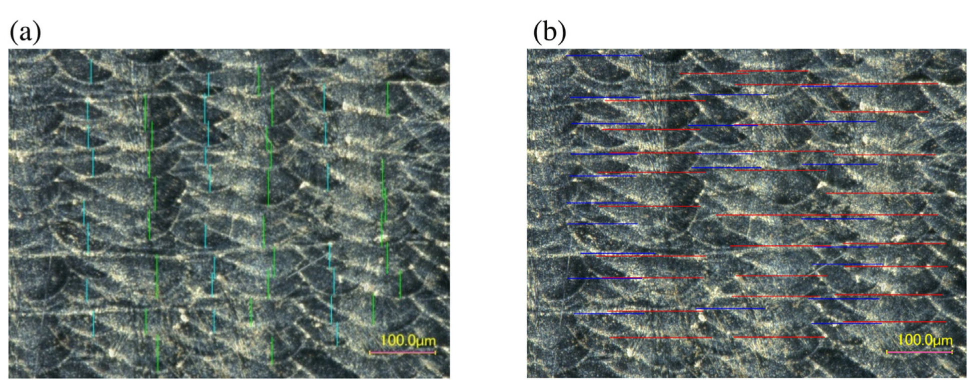

Fig. 14. Marked meltpool (a) width and (b) depth of Coupon 29 (XZ-plane).

Type-I meltpool, where the area being processed (points A and C in Figs. 12–13) is still within the heat-affected zone of the previous hatch scanning, and ii) a Type-II meltpool, where the area currently being processed (location B in Figs. 12–13) is no longer affected by the heat from the laser scanning of the previous hatch. Basically, the main reason for the Type-I meltpool to form is the heating of the previous scan line which leaves a large heat affective zone when the laser starts scanning on the second scan line, the meltpool portion on the left hand size of d dash line in Fig. 13 will be wider, however, the melt pool portion on the right hand size of d dash line should be narrower.

Type-I and Type-II meltpools can be formally defined as follows: define an YZ-plane at a specific x-location. The time elapsed between two consecutive meltpool footprints on this plane will vary as a function of the total laser scan distance in x direction between the two consecutive passes through this plane. For locations very close to the stripe boundaries, the difference in the elapsed times between Type-I and Type-II meltpools is the largest. This leads to different sized meltpools along this particular YZ-plane. The size of the meltpool will depend on the scanning direction. Meltpools at a location at the beginning of the stripe will be larger (Type-I) and meltpools at a location at the end of a processed stripe will be smaller (Type-II). The difference in meltpool sizes can be attributed to the presence of a heat-affected zone (HAZ) and rapid cooling times. A digital optical microscope was utilized to obtain images of the electro-polished surfaces from which the meltpool width and depth were measured. All the images utilized for analysis were captured in 1600 pixels × 1200 pixels resolution with 500× magnification. The images were measured using a built-in scale provided by the optical microscope (Fig. 14).

The number of pixels that makes up the length of the scale (100 μm) was counted to obtain a pixel-to-μm conversion ratio as 0.4184 μm/pixel. The width and depth of the meltpools were measured by drawing color-coded lines on the images and counting the number of pixels spanned by each individual line. Then, the measurements were converted to micrometers using the scale provided on the images. The resulting length measurement uncertainty (Type-B) due to the subjectivity of selecting appropriate pixels defining the meltpool boundaries is estimated as $u_{MP} = 3$ pixels × 0.4184 μm/pixel = 1.2552 μm by assuming a 67 percent probability that the meltpool boundaries exist within 3 pixel of the points selected (1.5 pixel per boundary) [25]. The width of Type-I and Type-II meltpools were marked using red (RGB = 255-0-0) and blue (RGB = 0-0-255), respectively (Fig. 14).

The depth of Type-I and Type-II meltpools were marked using green (R-G-B = 0-0-255) and cyan (R-G-B = 0-0-255), respectively (Fig. 14). A Matlab script was then used to automatically detect the colored lines and obtain the width and depth of each individual marked meltpool, using the scale as a reference. While each meltpool is measured only once for each image, multiple meltpool images of each coupon were analyzed following this methodology, and the results were compiled to obtain an average meltpool width and depth, with corresponding standard deviation. It was found that meltpool width changes considerably based on the type of meltpool. Meltpool depth also varies slightly between types, though there is overlap when accounting for standard deviation. Table 4 summarizes all meltpool width and depth by type for each coupon, with the respective standard deviation. The average values incorporated more than 30 individual measurements obtained from each coupon, resulting in a measurement uncertainty less than $u_{MP\_ave} = \left(3/\sqrt{30}\right)$ pixels × 0.418m/pixel = 0.229 μm for each coupon. The standard deviation columns in table represent the square root of the variance of those individual measurements.

The laser heating effect described in the previous section produces a notable effect on the geometrical shape of the meltpool as well. In particular, by analyzing the images obtained via optical microscopy, it was observed that the location along the *y*-axis at which the maximum melting depth occurs does not necessarily lie on the hatch centerline. Irregular meltpool shapes have been previously reported during L-PBF of nickel alloy 625 [2] and nickel alloy 738LC [7]. To quantify this effect, a measure of the meltpool shape was developed.

For this analysis, the cross-sectional (YZ-plane) view of the meltpool is considered. The meltpool width, *w*, and the distance from the edge of the meltpool farthest away from the previous hatch to the location at which the maximum melted depth is observed, *a*, are measured using the same methodology as before (Fig. 15a).

Then, a measure for the meltpool shape is defined as follows:

$$\varphi(a, w) = \frac{a - {}^{w}\!/_{2}}{{}^{w}\!/_{2}} = \frac{2a - w}{w} \tag{23}$$

With this definition, a way to determine how skewed the meltpool is has been established. If the meltpool is perfectly symmetrical about the *z*-axis, then $a = w/2$ and $\varphi = 0$, or 0%. On the contrary, if the meltpool is completely skewed towards the previous processed hatch due to the heat-affected zone, then $a \to w/2$, in which case $\varphi \to 1$, or 100%. In summary, this measure gives a value between 0 and 1 (or 0 and 100%) that quantifies how non-symmetrical the meltpool geometry is. This meltpool shape measure was applied to all coupons and an average measure and standard deviation of the meltpool shape for a specific set of process parameters was determined (Table 5). The main conclusion from this analysis is that beyond the variation in meltpool shape, Type-I and Type-II meltpools obtained via the same processing conditions have considerably different shapes.

3.3. Comparison of simulations with experiments

Simulation experiments following the Box-Behnken design of experiments were done in order to compare predicted meltpool geometry with measurements from fabricated test coupons. Meltpool width and depth are calculated from the simulation-based temperature profile for the third-hatch of a three-hatch simulation, at the beginning and the end of each track. This provides a width and depth estimation for Type-I and Type-II meltpools (Table 6).

It is now possible to compare the optical imaging analysis results with the simulation results. A straight forward way of comparing results is to look at meltpool geometry by type with respect to energy intensity. All simulation predictions for Type-I meltpool width are within one standard deviation of the measured average, except for the experimental unit processed with the highest energy density (Fig. 16).

Fig. 16b indicates that Type-II meltpool width is over-estimated by the simulation, but well within one standard deviation of the measured average using optical imaging. The linear fit for the measured data and the simulation results are essentially parallel to one another also within one standard deviation, which shows the accuracy of the prediction with simulation. Effect of increasing energy density on the meltpool depth is shown (Fig. 17) where measured and simulated meltpool depth values at various energy density levels obtained from experimental design are compared yielding good agreement between experimental and simulated results, especially for Type-II meltpools. Typically, to have a valid representation of the experimental measurement, an increase on meltpool width and depth should be seen when the energy density is increased.

4. Process Models

The Box-Behnken experimental design was utilized due to strict limitations in possible values of L-PBF process parameters and the restriction in the number of experimental units. However, this design is sufficient to obtain meaningful second-order response models [20]. The general form of the second order model is given as;

$$\eta = \beta_0 + \sum_{i=1}^{k} \beta_i x_i + \sum_{i=1}^{k} \beta_{ii} {x_i}^2 + \sum \sum_{i<j=2}^{k} \beta_{ij} x_i x_j + \varepsilon \tag{24}$$

where η is the output variable (e.g. density), *β*'s are the estimated parameters in the response, x_i's are the process variables, andε is the residual error. In the proposed experiment design, three process parameters are taken into consideration ($k = 3$): laser power, scan velocity, and hatch distance. Response surface regression models were obtained for relative density, meltpool width, depth and shape by utilizing experimental measurement results. Similarly, regression models were obtained for peak temperature and time above the melting temperature by using the results of

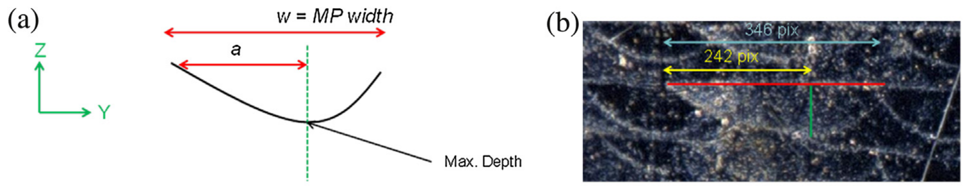

Fig. 15. (a) Maximum depth of melted material, (b) measurements for calculation of meltpool shape.

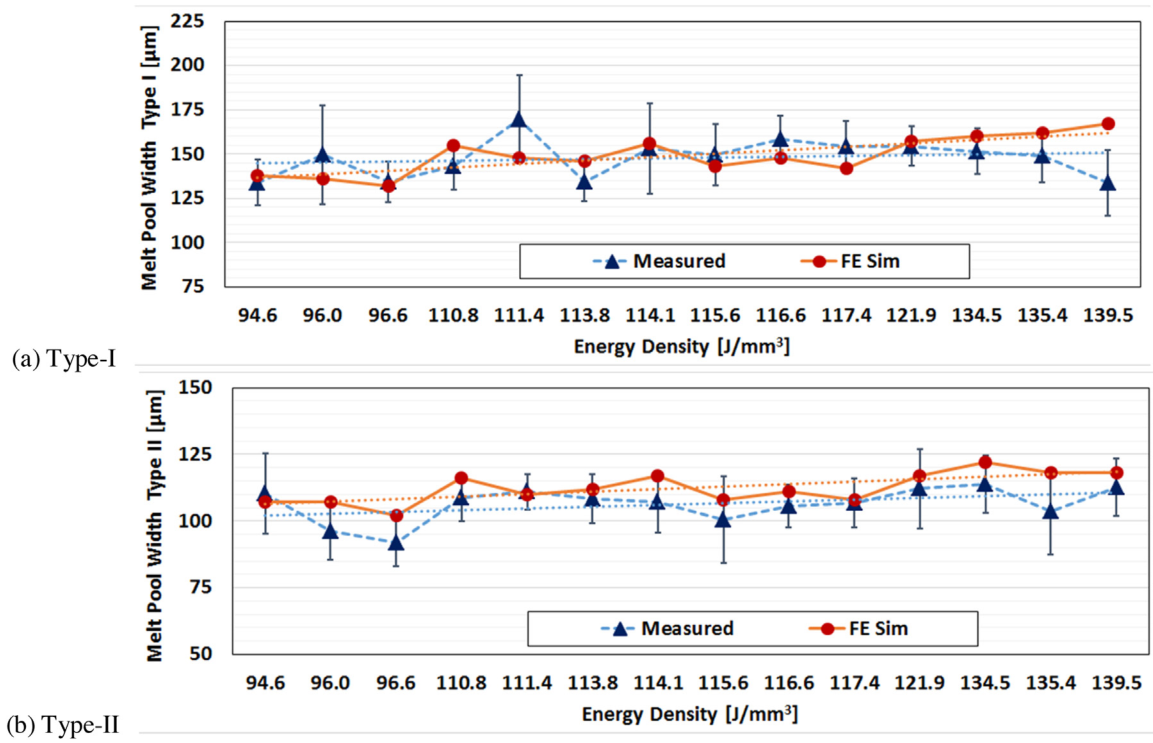

Fig. 16. Measured and predicted meltpool width.

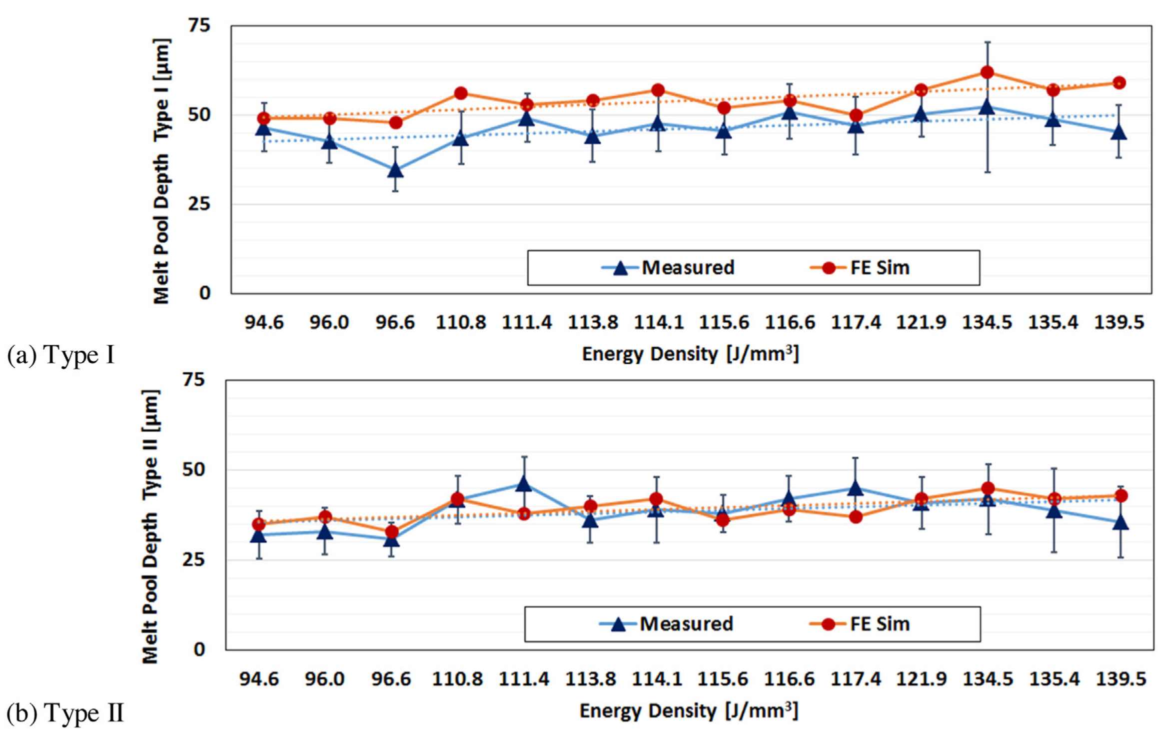

Fig. 17. Measured and predicted meltpool depth.

Table 4
Meltpool measurements (SSR = 90°).

Coupon	P [W]	v_s[mm/s]	h [mm]	Width-Avg. [μm]		Width-SD [μm]		Depth-Avg. [μm]		Depth-SD [μm]	
				I	II	I	II	I	II	I	II
01	169	875	0.10	134	92	12	9	35	31	6	5
04	195	875	0.10	170	111	25	7	49	46	7	8
06	182	875	0.09	149	101	17	16	45	38	7	5
08	182	725	0.11	153	107	25	12	48	39	8	9
09	195	800	0.11	143	109	13	9	44	42	7	7
12	182	725	0.09	134	113	18	11	45	36	7	10
14	182	800	0.10	132	109	11	10	44	38	7	6
15	182	800	0.10	128	105	12	11	40	33	9	6
16	195	725	0.10	152	114	13	11	52	42	18	10
17	182	800	0.10	143	112	10	7	48	38	6	7
18	182	875	0.11	134	110	13	15	47	32	7	7
20	169	725	0.10	159	106	13	8	51	42	8	6
21	169	800	0.09	154	107	14	9	47	45	8	9
23	169	800	0.11	150	96	28	11	43	33	6	6
29	195	800	0.09	149	103	15	16	49	39	7	12
35	195	800	0.10	155	112	11	15	50	41	6	7

Table 5
Meltpool shape measurements (SSR = 90°) by meltpool type.

				φ – Avg [%]		φ – SD [%]	
Coupon #	P [W]	v_s [mm/s]	h [mm]	Type-I	Type-II	Type-I	Type-II
01	169	875	0.10	10.0	2.2	3.1	2.9
04	195	875	0.10	16.1	13.4	2.5	2.4
06	182	875	0.09	19.4	15.3	3.1	2.7
08	182	725	0.11	12.6	12.7	4.3	4.7
09	195	800	0.11	11.8	10.5	4.2	4.0
12	182	725	0.09	15.0	2.7	3.2	4.7
14	182	800	0.10	10.9	1.0	4.0	4.1
15	182	800	0.10	16.3	6.7	3.7	4.5
16	195	725	0.10	9.5	11.5	3.6	4.1
17	182	800	0.10	8.6	0.4	2.7	4.5
18	182	875	0.11	7.1	0.1	2.4	3.1
20	169	725	0.10	11.0	2.6	3.6	6.1
21	169	800	0.09	23.4	11.5	5.1	6.4
23	169	800	0.11	9.1	0.2	2.8	6.4
29	195	800	0.09	21.0	6.0	5.2	5.5
35	195	800	0.10	5.4	3.5	2.5	3.3

Table 6
Simulated meltpool width and depth.

P [W]	v_s [mm/s]	h [mm]	E [J/mm^3]	Width[μm] Type-I	Width[μm] Type-II	Depth[μm] Type-I	Depth[μm] Type-II
169	875	0.10	96.57	132	102	48	33
195	875	0.10	111.43	148	110	53	38
182	875	0.09	115.56	143	108	52	36
182	725	0.11	114.11	156	117	57	42
195	800	0.11	110.80	155	116	56	42
182	725	0.09	139.46	167	118	59	43
182	800	0.10	113.75	146	112	54	40
195	725	0.10	134.48	160	122	62	45
182	875	0.11	94.55	138	107	49	35
169	725	0.10	116.55	148	111	54	39
169	800	0.09	117.36	142	108	50	37
169	800	0.11	96.02	136	107	49	37
195	800	0.09	135.42	162	118	57	42
195	800	0.10	121.88	157	117	57	42

physics-based simulation experiments. These models will be utilized in multi-objective optimization.

4.1. Relative density model

The Response Surface Methodology (RSM) analysis and Analysis of Variance (ANOVA) were performed using R statistical software for analysis of coupons fabricated using both SSR = 90° and 67° independently. The statistical model provides the estimates for the β_i's, where i = 1,2,3 correspond to laser power, scan velocity, and hatch distance, respectively. These coefficients are presented in Table 7. The R^2 values for the models are 0.9891 and 0.9919, for SSR = 90° and SSR = 67°, respectively, which indicates that fit between the data and the model is excellent. The results show that power and velocity are significant contributors to relative density of coupons fabricated. Especially, velocity appears to be the most significant term. It is also worth noting that the power-velocity interactions are significant. Additionally, response surface plots are generated using this model (Figs. 18–19). It can be seen that the densest coupons are obtained at a non-linear combination of power, velocity and hatch

Table 7
Relative density model approximation ($SSR = 90^\circ, 67^\circ$).

	SSR = 90°		SSR = 67°	
	Estimate	*p*-value	Estimate	*p*-value
β_0	98.093333	0.000000	98.23333	9.073e-15
β_1	0.946250	0.000027	0.872500	1.361e-05
β_2	0.008750	0.897819	0.141250	0.0416946
β_3	−0.392500	0.001767	−0.451250	0.0003329
β_{11}	−0.002917	0.976780	0.107083	0.2199178
β_{22}	−1.237917	0.000048	−1.100417	2.908e-05
β_{33}	−0.195417	0.095705	−0.230417	0.0295457
β_{12}	0.487500	0.003136	0.370000	0.0039632
β_{13}	0.090000	0.370999	0.105000	0.2119534
β_{23}	0.160000	0.141146	0.117500	0.1703002

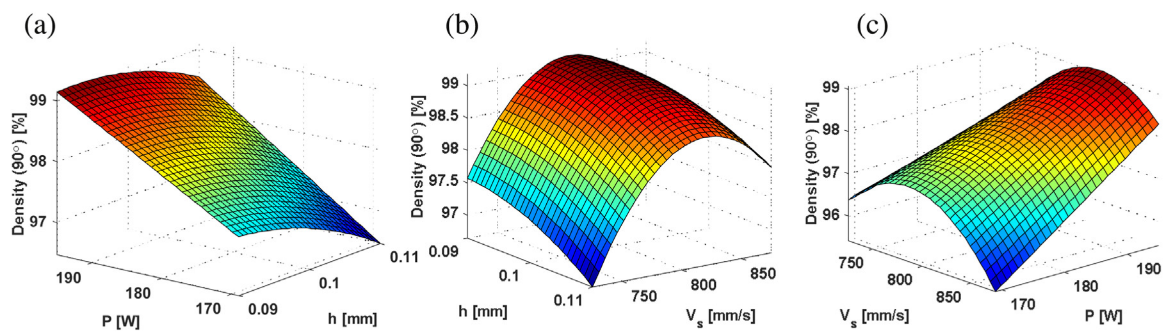

Fig. 18. Surface plots for relative density, $SSR = 90^\circ$ (a) $v_s = 800$ mm/s, (b) $P = 195$W, (c) $h = 0.1$ mm.

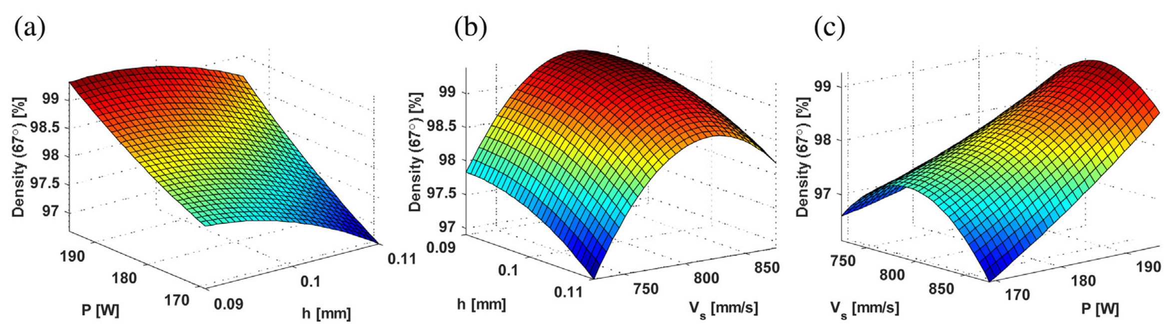

Fig. 19. Surface plots for relative density, $SSR = 67^\circ$ (a) $v_s = 800$ mm/s, (b) $P = 195$W, (c) $h = 0.1$ mm.

distance. Least dense coupons are obtained by implementing low power, highest velocity, and the largest hatch distance.

4.2. Meltpool width, depth, and shape models

This subsection provides a complete analysis using response surface methodology for the four measured outputs that describe the size of the meltpool: meltpool width (Types-I and II) and meltpool depth (Types-I and II) as functions of the same input process variables for $SSR = 90^\circ$. A table providing the estimated coefficients from fitting a quadratic model with interactions to the measured data is provided for each of the measured outputs, along with the specific process parameters that maximize said output within the explored range. Meltpool width models for Type-I and Type-II are given in Table 8. The R^2 value for Type-I model is 0.812, which indicates that the measured data is in acceptable agreement with the fitted model where as R^2 value for Type-II model is 0.8495, which indicates that the model is an acceptable fit for the measured data.

The ANOVA results show that power-squared and power-velocity interaction are the only significant factors in determining width for Type-I meltpools. The stationary, or optimal point, which maximizes Type-I meltpool width within the given range of process parameters is given by $P = 183$W, $v_s = 774$ mm/s, $h = 0.09$ mm.

The width of Type-II meltpools behaves significantly differently than of Type-I meltpools. In this case, power-velocity and power-hatch distance interactions are seen to be significant according to the ANOVA analysis. Therefore, not only does meltpool geometry showcase a dynamic behavior, but the characteristics of this behavior, as described by process parameters, change based on the location of the meltpool along the scanned track. The stationary, or optimal point, which maximizes Type II meltpool is given by $P = 192$W, $v_s = 767$ mm/s, $h = 0.10$ mm. Figs. 20–21 show response surface plots in which the quadratic behavior of the process can be seen clearly where meltpool width behavior varies significantly from Type-I and Type-II.

Meltpool depth models for Type-I and Type-II are given in Table 9. The R^2 value for the Type-I model is 0.5651, which indicates that the model is not a very good fit for the data whereas R^2 value for the Type-II model is 0.8682, which indicates that the model fits the measured data well. The ANOVA results for Type-I meltpool depth show that there are no significant factors in the quadratic model. However, the ANOVA results for Type-II meltpool depth show that power, power-squared, and power-velocity and

Table 8
Meltpool width model approximation ($SSR = 90^\circ$).

	Width (Type-I)		Width (Type-II)	
	Estimate	*p*-value	Estimate	*p*-value
β_0	134.3333	1.177e-06	108.66667	8.49e-08
β_1	2.1250	0.50836	4.50000	0.02512
β_2	−1.3750	0.66440	−3.25000	0.07140
β_3	−0.7500	0.81162	−0.25000	0.86757
β_{11}	12.9583	0.03191	−3.48533	0.15999
β_{22}	6.4583	0.20155	0.54167	0.80645
β_{33}	1.7083	0.71343	−1.45833	0.51773
β_{12}	10.7500	0.05148	2.75000	0.23044
β_{13}	−0.5000	0.91033	4.25000	0.08866
β_{23}	−8.5000	0.10020	3.75000	0.12174

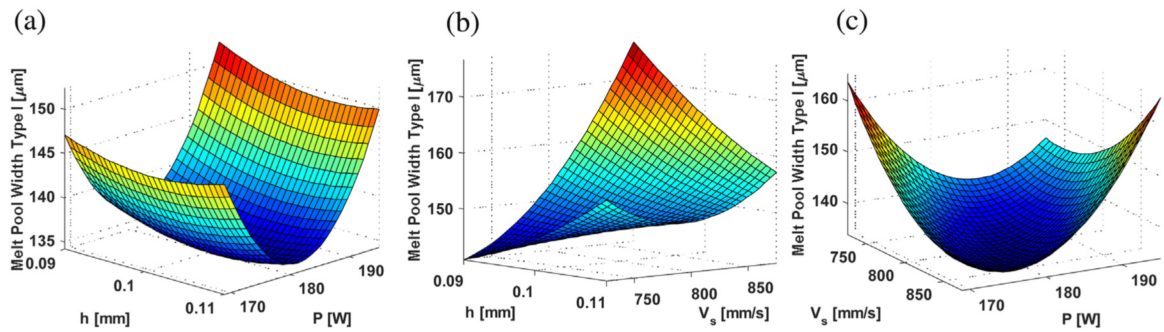

Fig. 20. Surface plots for meltpool width (Type-I) (a) $v_s = 800$ mm/s, (b) $P = 195$W, (c) $h = 0.1$ mm.

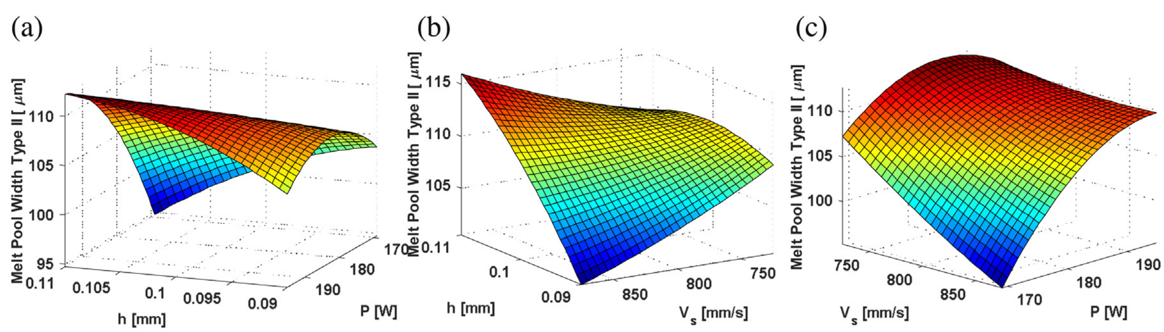

Fig. 21. Surface plots for meltpool width (Type-II) (a) $v_s = 800$ mm/s, (b) $P = 195$W, (c) $h = 0.1$ mm.

Table 9
Meltpool depth model approximation.

	Depth (Type-I)		Depth (Type-II)	
	Estimate	*p*-value	Estimate	*p*-value
β_0	44.0000	1.796e-05	36.3333	3.337e-06
β_1	2.2523	0.2419	2.2500	0.07340
β_2	−2.500	0.2004	−1.500	0.19234
β_3	−0.500	0.7799	−1.500	0.19253
β_{11}	1.1250	0.6710	3.70833	0.05254
β_{22}	1.6250	0.5437	0.20833	0.89253
β_{33}	0.6250	0.8122	−0.29167	0.85012
β_{12}	3.2500	0.2333	3.7500	0.04473
β_{13}	−0.2500	0.9203	3.7500	0.04358
β_{23}	−0.2500	0.9210	−2.2500	0.17101

power-hatch distance interactions are all significant. Therefore, it can be concluded that power is the predominant factor in determining resulting meltpool depth. This result makes intuitive sense since Type-II meltpools, those occurring at the end of the scanned track, are the result of heating an area of the powder bed that has not been processed recently. Therefore, the effect of velocity and hatch distance (previously scanned hatches) should be minimal.

Figs. 22–23 show response surface plots for the quadratic process behavior. It is obvious that shallow (least deep) meltpools occur when low power and high velocity are utilized. Conversely, high power and low hatch distance lead to the deepest meltpools. The quadratic behavior is most noticeable in the power-hatch distance and power-velocity interactions. The velocity-hatch distance interaction is quasi-linear.

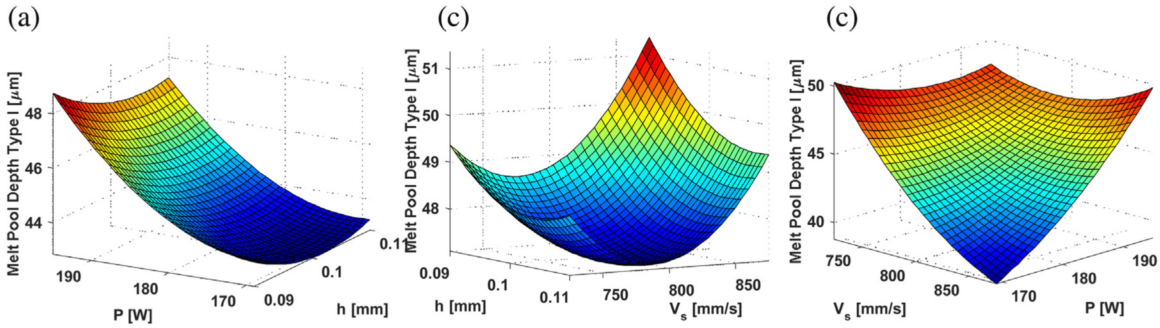

Fig. 22. Surface plots for meltpool depth (Type-I) (a) v_s = 800 mm/s, (b) P = 195W, (c) h = 0.1 mm.

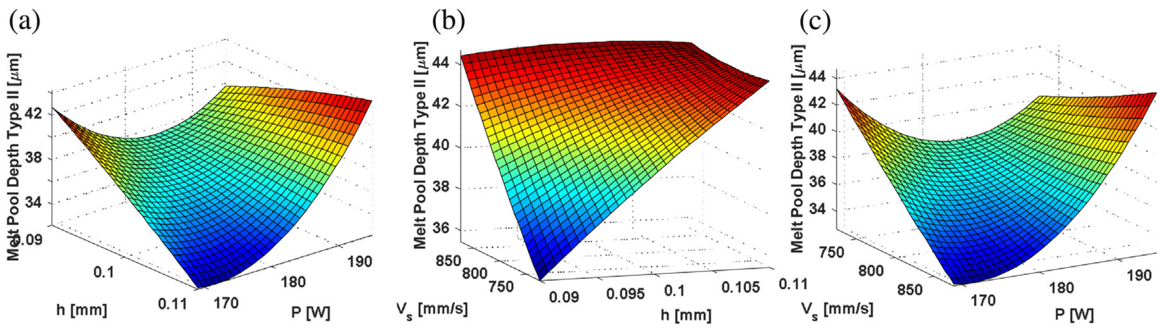

Fig. 23. Surface plots for meltpool depth (Type II) (a) v_s = 800 mm/s, (b) P = 195W, (c) h = 0.1 mm.

Table 10
Meltpool shape model approximation.

	MP Shape (Type I)		MP Shape (Type II)	
	Estimate	p-value	Estimate	p-value
β_0	11.92000	0.001190	2.70000	0.21477
β_1	0.61875	0.599289	3.12375	0.04365
β_2	0.56625	0.629810	0.19125	0.87594
β_3	−4.76500	0.007593	−1.50250	0.25328
β_{11}	1.26125	0.472699	2.03750	0.28781
β_{22}	−1.52875	0.389957	2.69750	0.17626
β_{33}	3.13375	0.111673	2.30500	0.23637
β_{12}	1.93750	0.269599	0.58000	0.73898
β_{13}	1.28500	0.447878	3.95750	0.06133
β_{23}	−2.50500	0.169465	−6.32250	0.01212

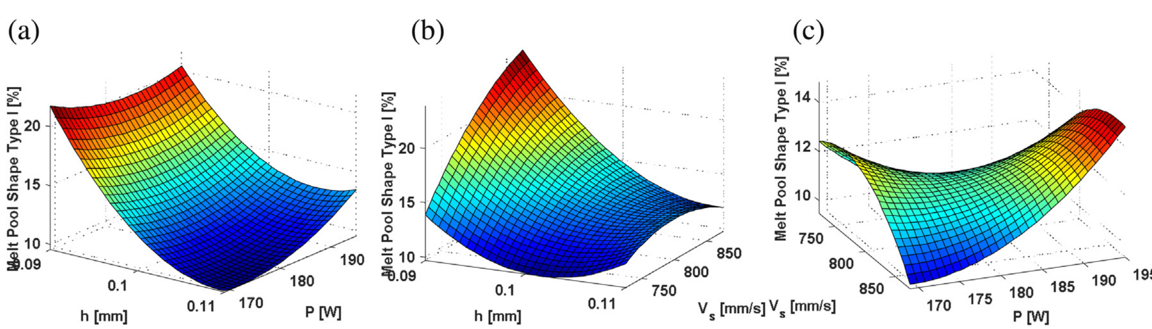

Fig. 24. Surface plots for meltpool shape (Type-I) (a) v_s = 800 mm/s, (b) P = 195W, (c) h = 0.1 mm.

Meltpool shape models for Type-I and Type-II are given in Table 10. The R^2 value for Type-I meltpool model is 0.8547, which indicates that the model is a good fit for the data. The R^2 value for Type-II meltpool model is 0.8734, which indicates a good fit. ANOVA results show that hatch distance is the most significant factor in Type-I meltpool shape. This result makes intuitive sense, since the deformation of the meltpool's shape is due to the heat affected zone generated by the scanning of the previous track. Therefore, it can be concluded that hatch distance is the predominant factor in determining resulting meltpool depth for Type-I. The effect of velocity and power should be smaller. ANOVA results for Type-II meltpool shape show that velocity-hatch distance interaction is the most significant factor. Other significant factors include power and power-hatch distance interaction. None of the quadratic terms are

Table 11
Simulation results for peak temperature and time above melting.

Coupon	P [W]	v_s [mm/s]	h [mm]	E [J/mm^3]	T_{peak} [K]	t_m [ms]
01	169	875	0.10	96.57	1985.7	0.25
04	195	875	0.10	111.43	2182.4	0.43
06	182	875	0.09	115.56	2124.1	0.34
08	182	725	0.11	114.11	2291.8	0.60
09	195	800	0.11	110.80	2280.2	0.56
12	182	725	0.09	139.46	2311.0	0.61
14–15–17	182	800	0.10	113.75	2226.7	0.47
16	195	725	0.10	134.48	2421.7	0.78
18	182	875	0.11	94.55	2076.8	0.33
20	169	725	0.10	116.55	2190.3	0.49
21	169	800	0.09	117.36	2121.6	0.34
23	169	800	0.11	96.02	2083.0	0.36
29	195	800	0.09	135.42	2338.5	0.56
34-35-36	195	800	0.10	121.88	2302.9	0.57

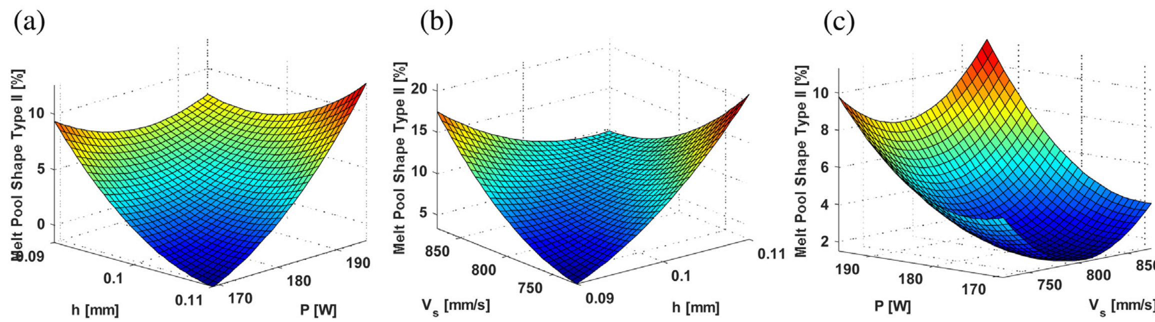

Fig. 25. Surface plots for meltpool depth (Type-II) (a) v_s = 800 mm/s, (b) P = 195W, (c) h = 0.1 mm.

Table 12
Peak temperature and time above melting temperature model approximation.

	T$_{peak}$ [K]		t$_m$ [ms]	
	Estimate	p-value	Estimate	p-value
β_0	2226.7	9.819e-13	0.4700	1.852e-8
β_1	105.2750	3.549e-07	0.11125	2.114e-6
β_2	−105.7250	3.474e-07	−0.14125	6.450e-7
β_3	−20.4250	0.001045	−2.82e-17	1.00000
β_{11}	−13.3875	0.029099	1.25e-3	0.85902
β_{22}	−18.2875	0.009012	1.625e-2	0.05932
β_{33}	−7.4875	0.150970	−1.625e-2	0.05932
β_{12}	−8.6750	0.096470	−2.75e-2	0.00785
β_{13}	−4.9250	0.298426	−5.00e-3	0.47149
β_{23}	−7.0250	0.158908	1.54e-18	1.00000

reported as significant, indicating that a linear model may be sufficient to characterize Type-II meltpool shape. By comparing to the Type-I meltpool shape results, it can be seen that the large deformations in meltpool shape seen in Type-I meltpools are not present in Type-II meltpools. Since Type-II meltpools are not occurring near a heat affected zone from a previous track, these exhibit a more symmetrical shape, more in line with what would be expected initially of this process. Figs. 24–25 show response surface plots obtained for meltpool shapes as function of process parameters.

4.3. Peak temperature and time above melting models

The physics-based modeling of the L-PBF process is used for simulation experiments. The goal was to provide information that cannot be easily measured accurately during the L-PBF process. Two specific variables; peak temperature (T_{peak}, the maximum temperature of the meltpool), and time above melting (t_m, amount of time a powder-bed location remains in liquid form, $T > T_l$) are selected at a location where the peak temperature is achieved corresponding to the beginning of the third-track (x = 0.05 mm), where a Type-I meltpool is observed. The peak temperatures and time above melting temperature predictions are obtained from the XY-plane simulation on the surface of the powder bed (Table 11).

ANOVA results for peak temperature and time above melting models are presented in Table 12. The R^2 value for the peak temperature model is 0.998 and for time above melting temperature is 0.997, which indicate that the fit between the data and the model is excellent. For peak temperature prediction, power and velocity appear to be the most significant terms. The only non-significant factors are the quadratic hatch distance factor, velocity-hatch distance, and power-hatch distance interactions.

Figs. 26–27 show response surface plots obtained by fixing one of the process parameters and varying the other two. It can be seen that the highest peak temperature and time above melting temperature is obtained at an almost linear combination of power, velocity, and hatch distance. Low peak temperatures and times above melting temperature are obtained by implementing low power, highest velocity, and largest hatch distance, but in such

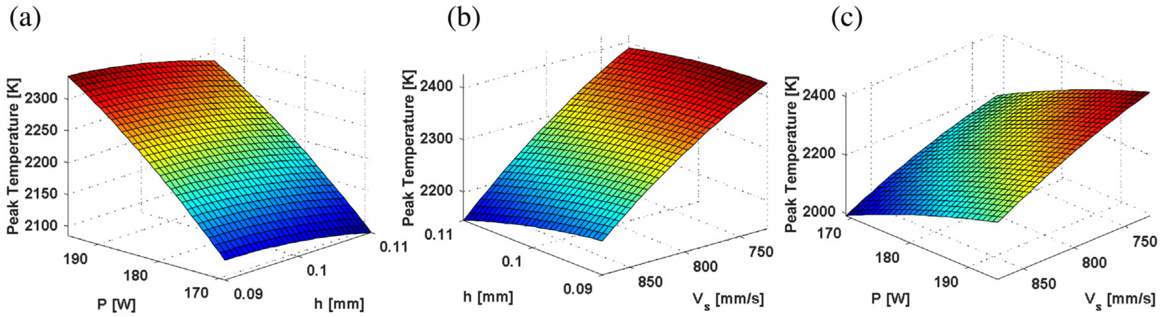

Fig. 26. Surface plots for peak temperature (a) $v_s = 800$ mm/s, (b) $P = 195$W, (c) $h = 0.1$ mm.

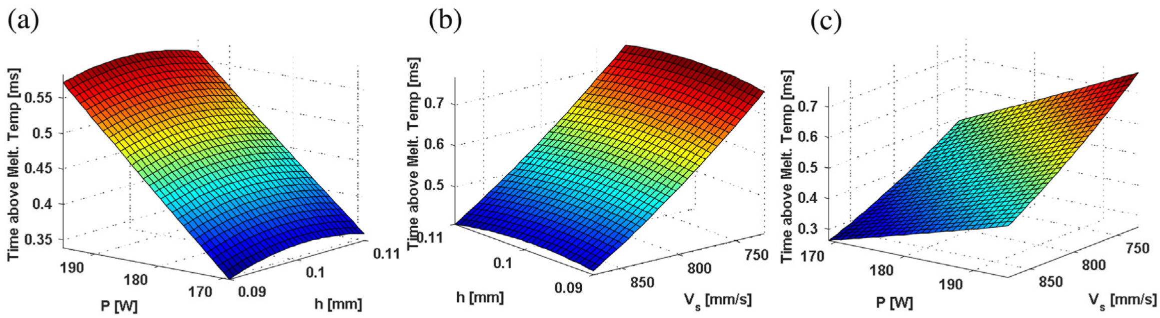

Fig. 27. Surface plots for time above melting temperature (a) $v_s = 800$ mm/s, (b) $P = 195$W, (c) $h = 0.1$ mm.

conditions incomplete fusion may occur in-between tracks based on the peak temperatures being lower than the liquidus temperature of the material.

5. Multi-Objective Optimization

Two techniques are utilized for optimization of process parameters: a multi-objective genetic algorithm (MOGA) [9] and a multi-objective particle swarm optimization (MOPSO) algorithm. MOPSO has been utilized extensively in multi-objective manufacturing optimization problems [26]. The first optimization problem deals with maximizing relative density (target relative density of 100%), maximizing processing rate, and minimizing energy density hence energy consumption. The second optimization problem looks to maximize relative part density, while minimizing peak temperature on the surface of the powder bed and minimizing the time above the melting temperature.

5.1. Optimization for maximum relative density, processing rate, minimum energy density

The first optimization problem uses objective functions obtained by using the results of the experimental analysis in L-PBF process. One of the key objectives is to obtain fully-dense parts. For this purpose, a measure of relative density to that of bulk nickel alloy 625, $_{\rho\mathrm{rel}}$, was developed where a relative density of 100% would be fully-dense and ideal. The predictive models for relative density obtained from the experimental analysis are given for 90° and 67° scan strategy respectively.

$$\begin{aligned}\rho_{rel,90} &= 30.2 - 0.39P + 0.2399v_s + 55h + 0.000017P^2 \\ &\quad -0.00022v_s^2 - 1954h^2 + 0.0005Pv_s + 0.692Ph + 0.213v_sh\end{aligned} \tag{25}$$

$$\begin{aligned}\rho_{rel,67} &= 44.3 - 0.548P + 0.2302v_s + 143h + 0.000634P^2 \\ &\quad -0.000196v_s^2 - 2304h^2 + 0.000379Pv_s + 0.808Ph + 0.1567v_sh\end{aligned} \tag{26}$$

Another objective is to minimize processing time, as L-PBF is currently a very time-consuming process, limited by the relatively low scan velocities. However, processing time is geometry-dependent and cannot be calculated reliably, especially for 67° scan strategy. This is because of the complexity involved in stripe rotation and resultant laser path that is internally determined by the machine control software that generates the path of scanning. Alternatively, response processing rate, R_p, can be defined as the volume of powder material processed per second [mm^3/s] and used as a measure to evaluate the performance of L-PBF.

$$R_p = v_s \times h \times s \tag{27}$$

Finally, the large amount of energy required by the L-PBF process can also be a concern. Therefore, energy density E [J/mm^3] applied can be used to control the amount of energy utilized by the process and minimizing this can lower the energy consumption.

These objectives are conflicting: maximum part density can be obtained for parts with low hatch distance and low velocity. Similarly, processing rate is maximized with high velocity and high hatch distance. Furthermore, utilizing higher power results in higher part density but also results in higher energy consumption. Therefore, a multi-objective optimization problem can be stated to address the optimization of conflicting objectives together with constraints in process parameters as follows. Maximize $\rho_{rel,\,90\,or\,67}$, maximize R_p, and minimize E:

$$\begin{aligned}&\text{Min.}\ \left\{-\rho_{rel,90\,or\,67}(P, v_s, h),\ -R_p(P, v_s, h),\ E(P, v_s, h)\right\} \\ &169 \le \mathrm{P} \le 195\mathrm{W} \\ &725 \le v_s \le 875\mathrm{mm/s} \\ &0.09 \le \mathrm{h} \le 0.11\mathrm{mm}\end{aligned} \tag{28}$$

This multi-objective problem is solved using two approaches. The first approach considers using the MOGA function *gamultiobj* in Matlab which utilizes Non-dominated Sorting Genetic Algorithm-II [9]. Table 13 summarizes the solver parameters chosen.

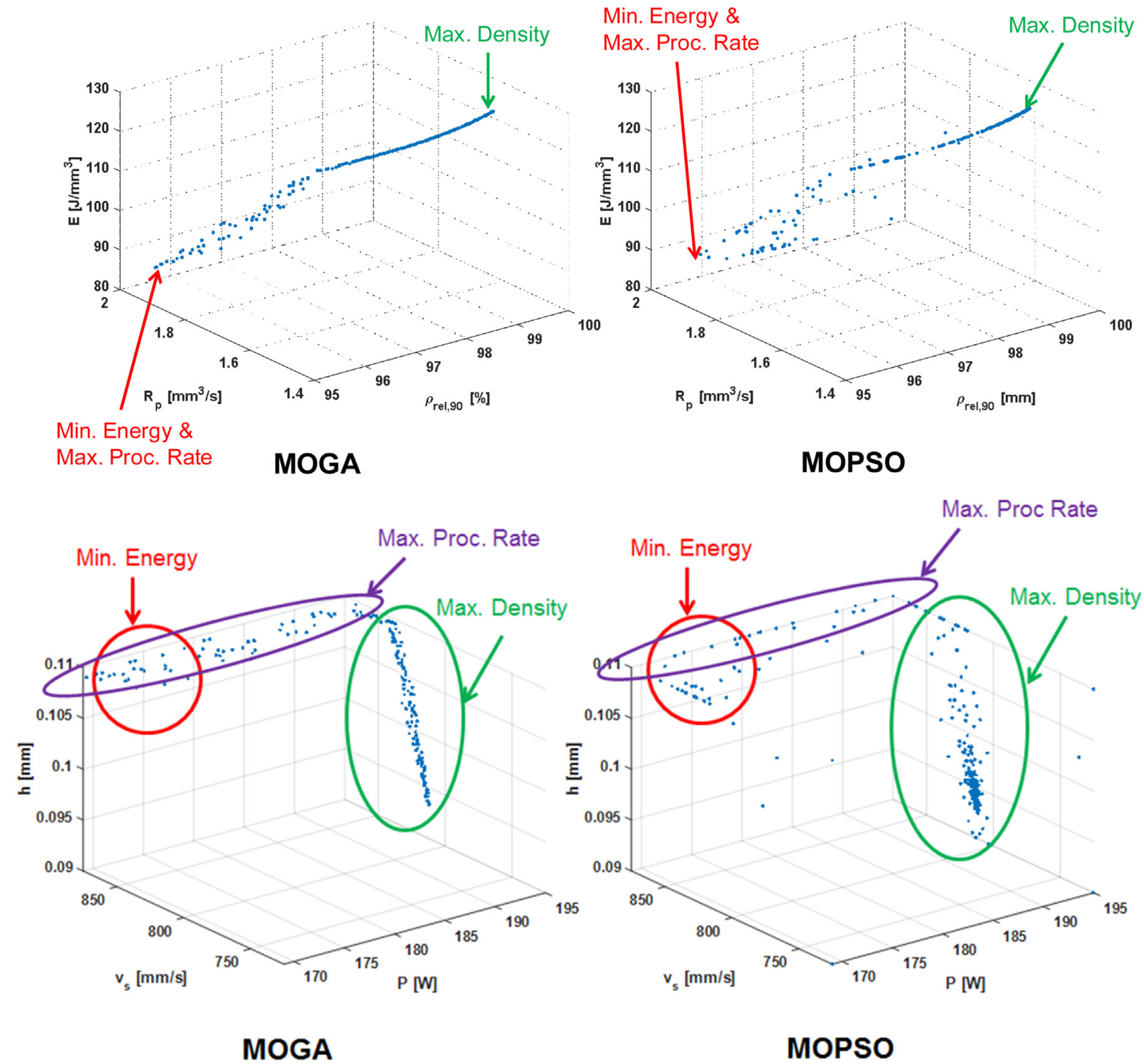

Fig. 28. Objective function (top) and decision variable (bottom) solution spaces for optimization of $_{\rho rel,90}$, R_p, and E.

Table 13
Solver parameters for MOGA.

Parameter	Setting
Population Size	500
Max. Generations	1000
Const. Tolerance	1e-6
Crossover Fraction	0.8
Elite Count	50
Pareto Fraction	0.35

Table 14
Solver parameters for MOPSO.

Parameter	Setting
Particles	500
Iterations	1000
Const. Tolerance	1e-6
Particle Accel. 1	2.02
Particle Accel. 2	2.02
Pareto Fraction	0.35

A second approach to solving the optimization problem consists of using Matlab to implement a MOPSO algorithm. Table 14 summarizes the process parameters utilized in the implementation. Notice that the number of particles and the number of iterations are equivalent to those used in MOGA.

Multi-objective optimization results obtained with MOGA and MOPSO are in figures where each point represents an optimal solution that forms part of the Pareto front. Fig. 28 shows the solution where $_{\rho rel,90}$ is maximized, R_p is maximized, and E is minimized. The results indicate that R_p achieves its optimal value at high hatch distance and high velocity combinations. Meanwhile, E achieves its optimal value for a smaller range, where high velocity (v_s = 875 mm/s), high hatch distance (h = 0.01 mm) and low power (P < 180W) are utilized. Maximum part density is obtained at maximum power. Fig. 29 shows a similar trend, indicating that there is no distinction between 67° and 90° scan strategies. In general, notice that the solutions obtained using MOGA and MOPSO are very similar to each other.

5.2. Optimization for maximum relative density, minimum peak temperature, and time above the melting

The second set of optimization problems utilizes objective functions obtained via predictive modeling using both the results from

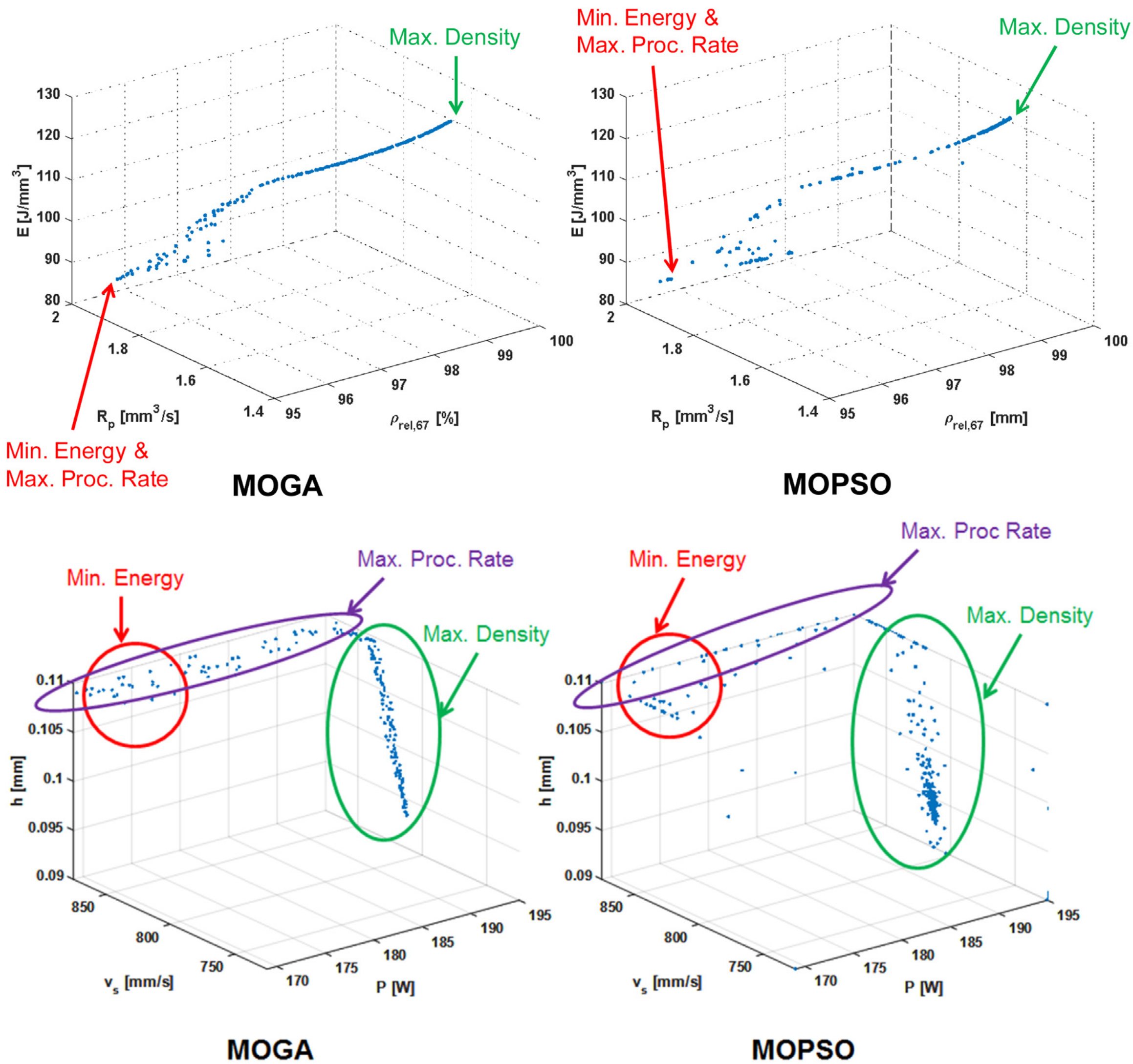

Fig. 29. Objective function (top) and decision variable (bottom) solution spaces for optimization of $_{\rho rel,67}$, R_p, and E.

the experimental analysis and physics-based simulations of L-PBF. First objective is to obtain fully-dense parts (100% relative density). The same predictive models to calculate the relative density of parts processed with 90° and 67° rotation between layers will be used in this analysis (Eqs. (25) & (26)). The predictive models for two key process parameters obtained from simulations, the peak temperature at the surface of the powder bed (T_{peak}) and the time spent by a particular location of the powder bed in liquid phase (t_m) are given as.

$$T_{peak} = 2226 + 105.275P - 105.725v_s - 20.425h - 13.3875P^2 - 18.2875v_s^2 - 7.4875h^2 - 8.675Pv_s - 4.925Ph - 7.025v_sh \quad (29)$$

$$t_m = 0.47 - 0.11125P - 0.14125v_s - 2.82 \times 10^{-17}h + 0.00125P^2 + 0.01625v_s^2 - 0.01625h^2 - 0.0275Pv_s - 0.005Ph - 1.54 \times 10^{-18}v_sh \quad (30)$$

These two parameters, along with heating and cooling times, have been identified as the keys to understanding how microstructure (and therefore, the mechanical properties) of L-PBF-produced parts vary with process parameters. The peak temperature must always be above the liquidus temperature of the material. Otherwise, full-melting of the powder material does not occur and incomplete fusion of powder material takes place.

These objectives are conflicting: maximum part density can be obtained for parts with low hatch distance and low velocity. Similarly, peak temperature is minimized with low power, high velocity and high hatch distance. Furthermore, utilizing higher power results in higher part density but also results in larger meltpools. Therefore, a location of the powder bed belongs to the meltpool for a longer period of time and t_m increases as more power is utilized. A multi-objective optimization problem can be stated as follows. Maximize $\rho_{rel,90or67}$, minimize T_{peak}, and minimize t_m:

$$\begin{aligned} &\text{Min.} \left\{-\rho_{rel,90or67}(P, v_s, h), T_{peak}(P, v_s, h), t_m(P, v_s, h)\right\} \\ &169 \le \text{P} \le 195\text{W} \\ &725 \le v_s \le 875\text{mm/s} \\ &0.09 \le \text{h} \le 0.11\text{mm} \end{aligned} \quad (31)$$

Multi-objective optimization results obtained with MOGA and MOPSO where each point represents an optimal solution to the problem where $_{\rho rel,90}$ is maximized, R_p is maximized, and E is minimized on the Pareto front are shown in Fig. 30. The results indicate that T_{peak} achieves its optimal value at high hatch distance

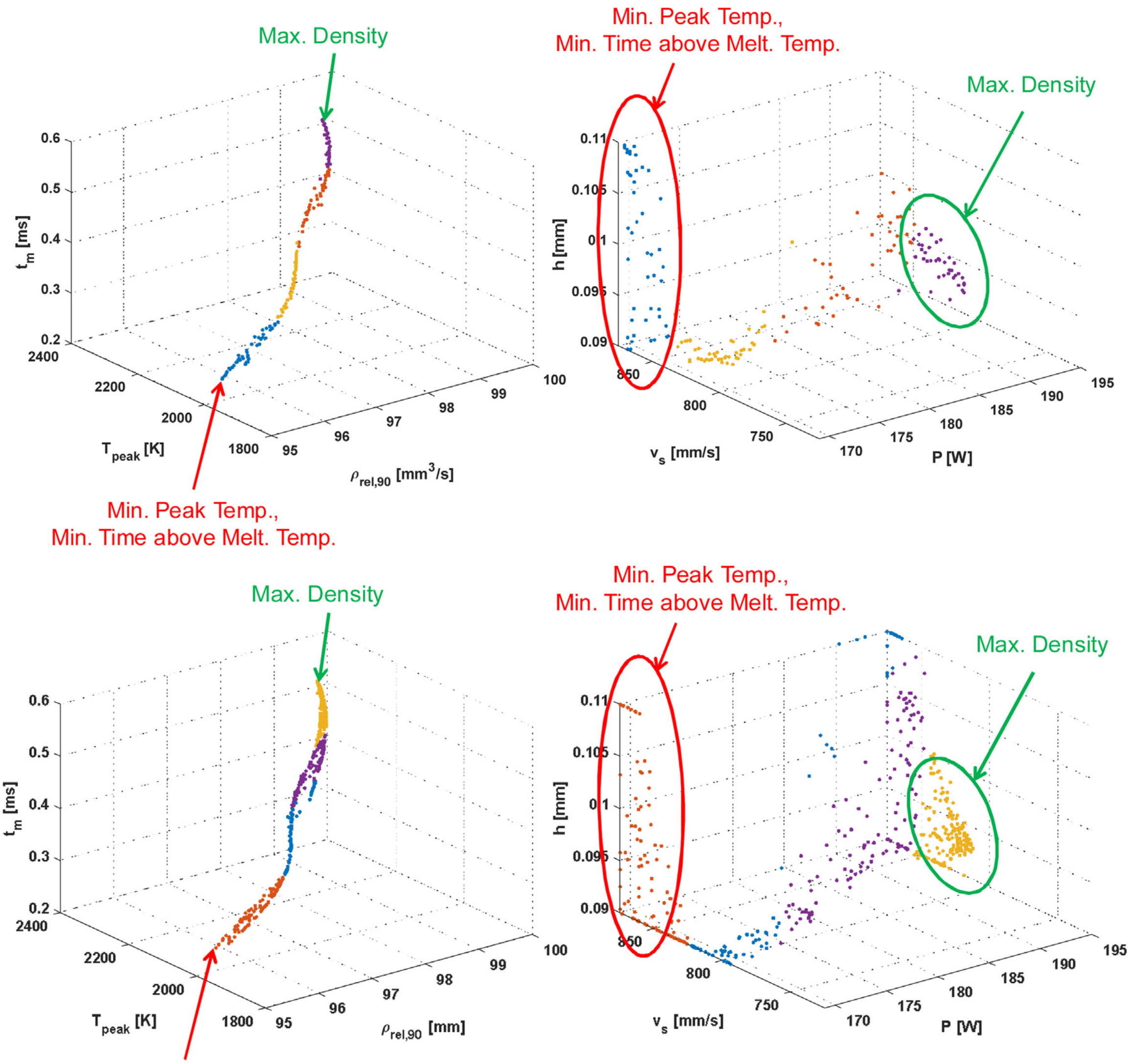

Fig. 30. MOGA (top) and MOPSO (bottom) solutions for optimization of $\rho_{rel,90}$, T_{peak}, and t_m showing the objective function value space (left) and the decision variable space (right).

and high velocity combinations. Similarly, t_m achieves its optimal value for the same range of process parameters, where high velocity (v_s = 875 mm/s), high hatch distance (h = 0.01 mm) and low power (P < 175 W) are utilized.

Fig. 31 shows the solution portraying a similar trend, indicating that there is no inherent difference in the optimization problem between 67° and 90° scanning strategy beyond the predicted values. The solution obtained with MOPSO contains a larger number of solutions in the intermediary region, the region between optimization of a single objective.

6. Conclusions

In this paper, 2-D Finite Element-based thermal and meltpool models (on the XY-, YZ- and XZ-planes) for laser powder bed fusion of nickel alloy 625 has been developed. Model results in meltpool size predictions for two distinct types (Type I and Type II meltpool) have been compared against the results of experimental analysis performed at various process settings. Peak temperature and time above melting temperature are identified as important process variables in L-PBF process as they may affect the quality of the powder material fusion. Predicted temperature variables have been utilized in optimization of process parameters for considering objectives such as minimizing peak temperature and time above melting temperature to avoid overheating while maximizing relative density of the part produced. Some of the major findings in the paper can be summarized as follows:

- Meltpool sizes and shapes are affected by subsequent scanning of the tracks due to heat affected zones.
- Meltpool depth cannot be measured easily during LPBF process but can be predicted by using thermal modeling for process planning purposes.
- Predicted peak temperatures and time above melting temperature allow a better understanding of the effect of various LPBF process energy densities and optimizing of the process parameters.

Acknowledgement

This project was supported by the National Institute of Standards and Technology, United States Department of Commerce, under the financial assistance number 70NANB14H227.

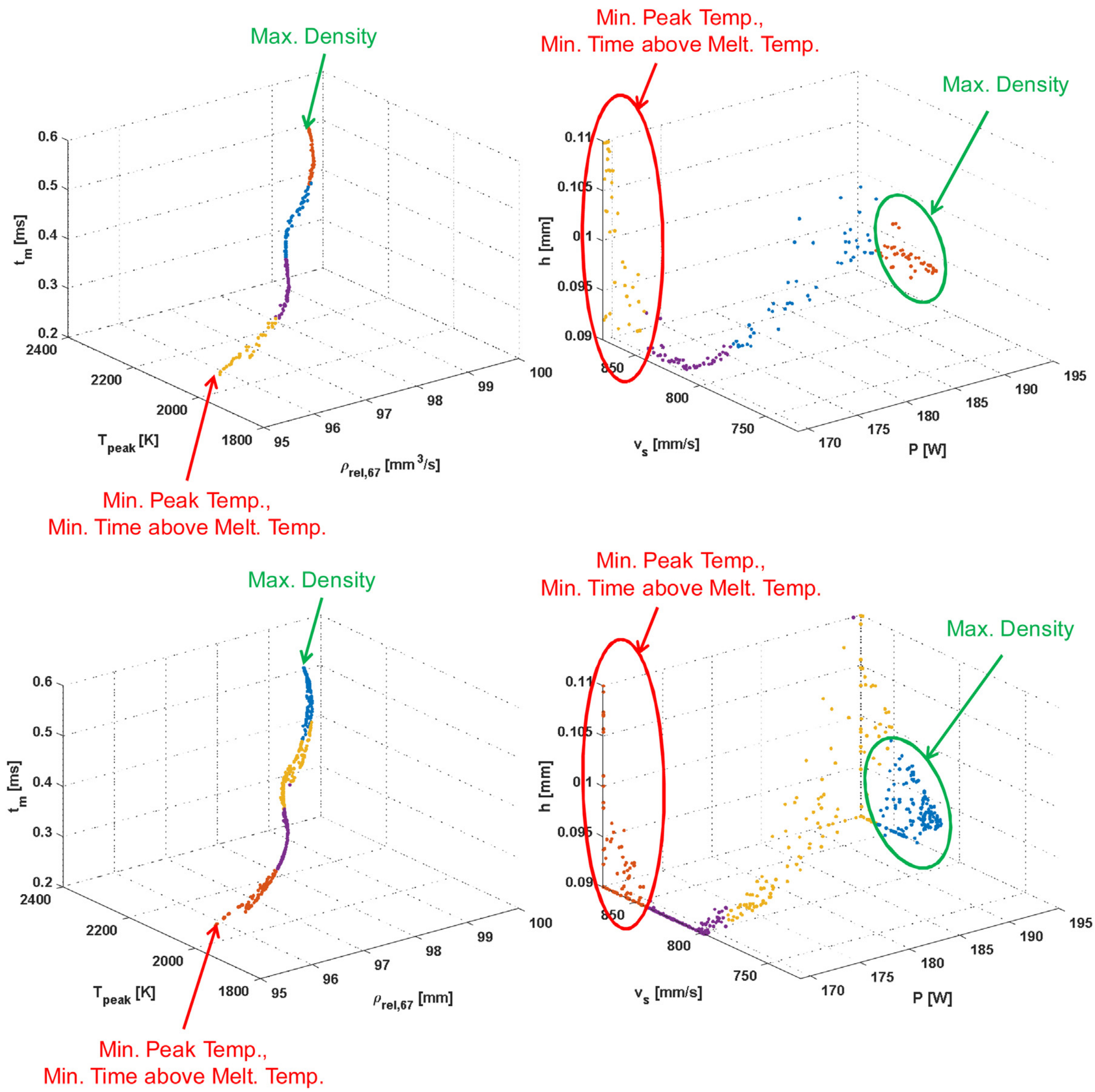

Fig. 31. MOGA (top) and MOPSO (bottom) solutions for optimization of ${}_{\rho\mathrm{rel},67}$, T_{peak}, and t_m showing the objective function value space (left) and the decision variable space (right).

References

[1] P. Aggarangsi, J.L. Beuth, M. Griffith, Melt pool size and stress control for laser-based deposition near a free edge, in: Proceedings of Solid Freeform Fabrication Symposium, University of Texas, Austin, TX, 2003, pp. 196–207.

[2] M.A. Anam, D. Pal, B. Stucker, Modeling and Experimental validation of Nickel-based super alloy (Inconel 625) made using Selective Laser Melting, in: Proc. 24th Annual Int. Solid Freeform Fabrication Symp.–An Additive Manufacturing Conf., Austin, TX, USA, 2013, pp. 463–473.

[3] J.-M. Bergheau, R. Fortunier, Finite element simulation of heat transfer, John Wiley & Sons, 2008.

[4] M. Boivineau, C. Cagran, D. Doytier, V. Eyraud, M.-H. Nadal, B. Wilthan, G. Pottlacher, Thermophysical properties of solid and liquid Ti-6Al-4 V (TA6 V) alloy, International Journal of Thermophysics 27 (2006) 507–529.

[5] E. Brinksmeier, G. Levy, D. Meyer, A. Spierings, Surface integrity of selective-laser-melted components, CIRP Ann. Manuf. Technol. 59 (2010) 601–606.

[6] L.N. Carter, C. Martin, P.J. Withers, M.M. Attallah, The influence of the laser scan strategy on grain structure and cracking behaviour in SLM powder-bed fabricated nickel superally, Journal of Alloys and Compounds 615 (2014) 338–347.

[7] M. Cloots, P.J. Uggowitzer, K. Wegener, Investigations on the microstructure and crack formation of IN738LC samples processed by selective laser melting using Gaussian and doughnut profiles, Mater. Des. 89 (2016) 770–784.

[8] L. Criales, Y.M. Arisoy, T. Özel, Sensitivity Analysis of Material and Process Parameters in Finite Element Modeling for Selective Laser Melting of Inconel 625, International Journal of Advanced Manufacturing Technology (2016), http://dx.doi.org/10.1007/s00170-015-8329-y.

[9] K. Deb, A. Pratap, S. Agarwal, T. Meyarivan, A fast and elitist multiobjective genetic algorithm: NSGA-II, IEEE Transactions on Evolutionary Computation 6 (2002) 182–197.

[10] R. Engeli, T. Etter, S. Hover, K. Wegener, Processability of different IN738LC powder batches by selective laser melting, Journal of Materials Processing Technology 229 (2016) 484–491.

[11] A. Foroozmehr, M. Badrossamay, E. Foroozmehr, S.I. Golabi, Finite element simulation of selective laser melting process considering optical penetration depth of laser in powder bed, Mater. Des. 89 (2016) 255–263.

[12] A. Gusarov, I. Smurov, Modeling the interaction of laser radiation with powder bed at selective laser melting, Phys. Procedia 5 (2010) 381–394.

[13] A. Gusarov, I. Yadroitsev, P. Bertrand, I. Smurov, Heat transfer modelling and stability analysis of selective laser melting, Applied Surface Science 254 (2007) 975–979.

[14] A. Hussein, L. Hao, C. Yan, R. Everson, Finite element simulation of the temperature and stress fields in single layers built without-support in selective laser melting, Mater. Des. 52 (2013) 638–647.

[15] Q. Jia, D. Gu, Selective laser melting additive manufacturing of Inconel 718 superalloy parts: Densification, microstructure and properties, Journal of Alloys and Compounds 585 (2014) 713–721.

[16] S. Kolossov, E. Boillat, R. Glardon, P. Fischer, M. Locher, 3D FE simulation for temperature evolution in the selective laser sintering process, International Journal of Machine Tools and Manufacture 44 (2004) 117–123.

[17] B. Lane, S. Moylan, E. Whitenton, L. Ma, Thermographic Measurements of the Commercial Laser Powder Bed Fusion Process at NIST, in: Proc. 26th Annual

Int. Solid Freeform Fabrication Symp. -An Additive Manufacturing Conf., Austin, TX, 2015.
[18] C. Montgomery, J. Beuth, L. Sheridan, N. Klingbeil, Process Mapping of Inconel 625 in Laser Powder Bed Additive Manufacturing, in: Proc. 26th Annual Int. Solid Freeform Fabrication Symp.–An Additive Manufacturing Conf., Austin, TX, USA, 2015, pp. 1195–1204.
[19] L. Murr, S. Gaytan, D. Ramirez, E. Martinez, J. Hernandez, K. Amato, P. Shindo, F. Medina, R.1 Wicker, Metal fabrication by additive manufacturing using laser and electron beam melting technologies, J. Mater. Sci. Technol. 28 (2012) 1–14.
[20] R.H. Myers, D.C. Montgomery, C.M. Anderson-Cook, Response Surface Methodology: Process and Product Optimization Using Designed Experiments, John Wiley & Sons, 2009.
[21] NIST, Box-Behnken Designs, 2015, Available at: http://www.itl.nist.gov/div898/handbook/pri/section3/pri3362.htm2015 (Accessed on 5 April 2016).
[22] C. Qiu, C. Panwisawas, M. Ward, H.C. Basoalto, J.W. Brooks, M.M. Attallah, On the role of melt flow into the surface structure and porosity development during selective laser melting, Acta Materialia 96 (2015) 72–79.
[23] I. Roberts, C. Wang, R. Esterlein, M. Stanford, D. Mynors, A three-dimensional finite element analysis of the temperature field during laser melting of metal powders in additive layer manufacturing, International Journal of Machine Tools and Manufacture 49 (2009) 916–923.
[24] B. Song, S. Dong, B. Zhang, H. Liao, C. Coddet, Effects of processing parameters on microstructure and mechanical property of selective laser melted Ti6Al4V, Mater. Des. 35 (2012) 120–125.
[25] B.N. Taylor, C.E. Kuyatt, Guidelines for Evaluating and Expressing the Uncertainty of NIST Measurement Results. NIST Technical Note 1297, 1994, http://www.nist.gov/pml/pubs/tn1297/ (Accessed on 28 March 2016).
[26] T. Thepsonthi, T. Özel, Multi-objective process optimization for micro-end milling of Ti-6Al-4V titanium alloy, International Journal of Advanced Manufacturing Technology 63 (2012) 903–914.
[27] M. Van Elsen, M. Baelmans, P. Mercelis, J.-P. Kruth, Solutions for modelling moving heat sources in a semi-infinite medium and applications to laser material processing, International Journal of Heat and Mass Transfer 50 (2007) 4872–4882.
[28] Z. Wang, K. Guan, M. Gao, X. Li, X. Chen, X. Zeng, The microstructure and mechanical properties of deposited-IN718 by selective laser melting, Journal of Alloys and Compounds 513 (2012) 518–523.
[29] C.B. Williams, J.K. Cochran, D.W. Rosen, Additive manufacturing of metallic cellular materials via three-dimensional printing, International Journal of Advanced Manufacturing Technology 53 (2011) 231–239.